

Ab Initio Study of a Molecular Crystal for Photovoltaics: Light Absorption, Exciton and Charge Carrier Transport

Andriy Zhugayevych,[†] Olena Postupna,^{†,‡} Ronald C. Bakus II,[§] Gregory C. Welch,[§] Guillermo C. Bazan,^{*,§} and Sergei Tretiak^{*,†}

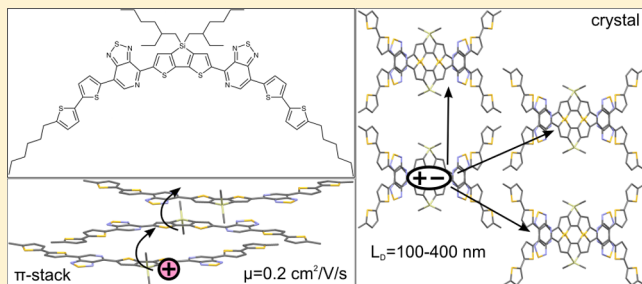
[†]Theoretical Division, Center for Nonlinear Studies and Center for Integrated Nanotechnologies, Los Alamos National Laboratory, Los Alamos, New Mexico 87545, United States

[‡]Department of Chemistry, University of Rochester, Rochester, New York 14627, United States

[§]Departments of Materials and Chemistry and Biochemistry, Center for Polymers and Organic Solids, University of California, Santa Barbara, California 93106, United States

S Supporting Information

ABSTRACT: Using ab initio methods we examine the molecular and solid-state electronic properties of a recently synthesized small-molecule donor, *p*-DTS(PTTh₂)₂, which belongs to the dithienosilole-pyridylthiadiazole family of chromophores. In combination with the PC₇₀BM acceptor, *p*-DTS(PTTh₂)₂ can be used to fabricate high-efficiency bulk heterojunction organic solar cells. A precise picture of molecular structure and interchromophore packing is provided via a single-crystal X-ray diffraction study; such details cannot be easily obtained with donor materials based on conjugated polymers. In first-principles approaches we are limited to a single-crystallite scale. At this scale, according to our investigation, the principal properties responsible for the high efficiency are strong low-energy light absorption by individual molecules, large exciton diffusion length, and fast disorder-resistant hole transport along π -stacks in the crystallite. The calculated exciton diffusion length is substantially larger than the average crystallite size in previously characterized device active layers, and the calculated hole mobility is 2 orders of magnitude higher than the measured device-scale mobility, meaning that the power conversion “losses” on a single-crystallite scale are minimal.



I. INTRODUCTION

Organic photovoltaic^{1–15} (OPV) devices are of interest in academia and industry because of their potential to provide cost-effective energy generating sources. Organic semiconductors typically are good light absorbers so that the OPV layers are relatively thin (100–200 nm). Optical excitation leads to the formation of a strongly bound electron–hole pair called an exciton. Current is produced through exciton dissociation at heterojunctions between two materials, resulting in the generation of free electron and hole carriers: the electron goes to the material with the higher electron affinity (acceptor), while the hole resides in the material with the lower ionization potential (donor). To increase the donor/acceptor interfacial area and shorten the exciton pathway toward the dissociation, the so-called bulk heterojunction (BHJ) geometry is used,¹⁶ where the donor and acceptor materials form a blend with interpenetrating domains of the two components, each of which directs charge to the corresponding electrode.

From the theoretical point of view, significant first-principles investigations of the processes of light absorption and exciton and charge carrier transport have been published and reviewed.^{17–29} These studies aim to understand the basic physical processes occurring in the active layer thin films and

rationalize the experimental findings down to the molecular scale, with the ultimate goal of providing predictive tools.¹⁷ Despite progress, an accurate theoretical description is still challenging because of the multiscale nature of the problem³⁰ and the inexact details concerning the BHJ structure and the internal organization within the donor and acceptor phases. Even at the single-molecule scale level, ab initio methods are usually limited to density functional theory (DFT), or perturbation theory at most (MP2), because of the size of the system, typically involving hundreds of atoms. Moreover, both DFT and MP2 are prone to errors in describing large π -conjugated systems especially with respect to excited states.^{31–35} Strong vibronic couplings and highly anharmonic torsional modes are typical for materials used in OPVs,^{18,36–38} which significantly complicate the first-principle description. On a larger, mesoscopic scale, the range of available theoretical and experimental methods is limited so that even the geometrical structure of an active layer is difficult to determine with atomic resolution.

Received: November 2, 2012

Revised: February 6, 2013

Published: February 17, 2013

The majority of solution-processed BHJ OPVs studied thus far are based on conjugated polymer donors and fullerene acceptors.^{7,39–41} More recently, small-molecule donors have been reported with efficiencies that are approaching those of their polymeric counterparts.^{42–45} For example, solar cells based on molecular donors containing dithienosilole-pyridylthiadiazole moieties,⁴⁶ such as *p*-DTS(PTTh₂)₂ in Figure 1,

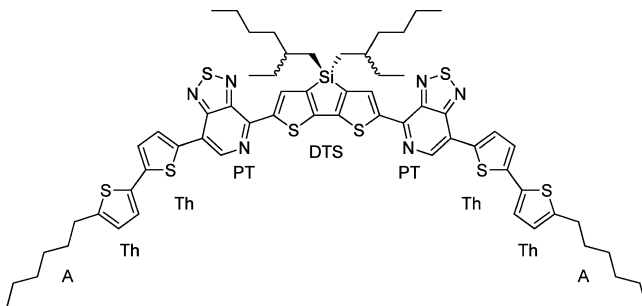


Figure 1. Chemical structure of the *p*-DTS(PTTh₂)₂ molecule; A corresponds to aliphatic chains, DTS, PT, and Th denote dithienosilole, pyridylthiadiazole, and thiophene moieties, respectively.

display power conversion efficiencies as high as 6.7%.⁴⁷ Attractive features of molecular systems include their well-defined structure, ease of functionalization, and the opportunity for purification using standard organic chemistry techniques.⁴⁸ The discrete nature of small molecules allows for a larger breadth of characterization procedures, leading to unprecedented insight into the structural characterization of chromophores within the donor phase. In the case of *p*-DTS(PTTh₂)₂ one observes by transmission electron microscopy formation of crystalline domains, the size of which correlates with device performance.⁴⁷

In this contribution we take advantage of a crystallographically determined structure of *p*-DTS(PTTh₂)₂ to perform theoretical investigation of exciton and charge transport on a single-crystallite scale. Having an experimentally determined picture of the molecular conformation and how these subunits pack within the lattice, our theoretical characterization provides insight into how given particular molecular assembly determines bulk properties. No analogous level of structural insight exists for the narrow band gap conjugated polymer donor materials due to the strict challenge of obtaining polymer single crystals.

The paper is organized as follows. In section II we describe the computational methodology. Section III provides an analysis of the geometry, electronic structure and excitations, and calculations of exciton diffusion and charge carrier mobility. Finally we discuss the trends that emerge, and summarize our results in section IV.

II. COMPUTATIONAL METHODOLOGY

The electronic structure calculations are based on DFT methodology applied to the ground state of neutral and charged molecular systems. Molecular excited states are calculated by taking advantage of the time-dependent DFT (TDDFT) approach. All calculations are carried out with the Gaussian 09 program⁴⁹ using CAM-B3LYP density functional⁵⁰ and the 6-31G* basis set.⁵¹ CAM-B3LYP is a hybrid long-range corrected functional, providing correct description of the neutral excitations³³ and charged states³⁸ in extended π -conjugated systems like the one investigated in this paper.

Description of long-range intermolecular couplings necessitates inclusion of polarization functions into the basis set (6-31G*). Nevertheless, the structure of the modeled absorption spectrum is described sufficiently well with a smaller basis set, 6-31G. To compare calculated and experimentally observed spectra measured in chloroform solution, the solvent effects are taken into account using the conductor-like polarizable continuum model^{52–54} (CPCM) with the dielectric constants $\epsilon_{\text{static}} = 4.7$ and $\epsilon_{\text{optic}} = 2.1$. The static dielectric constant of the studied crystal ($\epsilon_{\text{static}} = 3.8$) was estimated by the Clausius–Mossotti relation. Therefore, the calculations in chloroform can mimic the dielectric effects of the crystalline environment, which is important for estimating the total energy of a charged state.

To study exciton and charge transport in the crystal, we rely on hopping-like models and start with calculating the transition rates between molecules. The assumption of localization of electronic excitations on a single chromophore is an approximation, and more delocalized Frenkel-like excitons⁵⁵ may exist in the crystal (see pp S10–S11 of the Supporting Information for details). Upon our approximation, the exciton-transfer rates between a pair of molecules are calculated by a Förster-like formula:^{19,26,56}

$$w = \frac{2\pi}{\hbar} |V|^2 J \quad (1)$$

where V is the exciton intermolecular coupling and J is the spectral overlap. The methodology of estimating exciton couplings is described on pp S7–S8 of the Supporting Information: it is similar to taking the half-energy split between the two lowest excited states for the molecular dimer^{57,58} but, additionally, is able to treat a case of nonequivalent monomers. The spectral overlap is given by

$$J = \int \rho_{\text{emi}}(E)\rho_{\text{abs}}(E) \, dE \quad (2)$$

where $\rho_{\text{emi}}(E) \sim I_{\text{emi}}(E)/E^3$ and $\rho_{\text{abs}}(E) \sim I_{\text{abs}}(E)/E$ are normalized (integrated to unity) vibrationally resolved emission and absorption spectral line shapes. For the latter we use the experimentally measured fluorescence excitation and emission spectra,^{59,60} because current DFT methods lack quantitative accuracy in estimating J (see Figure S4 and Table S3 of the Supporting Information).

Charge carrier transfer rates are calculated by the Marcus formula,¹⁸ which for zero field and identical molecules reads

$$w = |t|^2 \sqrt{\frac{\pi}{\hbar^2 \lambda kT}} \exp\left(-\frac{\lambda}{4kT}\right) \quad (3)$$

Here t is the electron-transfer integral, λ is the internal reorganization energy, and T is the room temperature. The internal reorganization energy is calculated from the DFT-derived total energies:¹⁹

$$\lambda = E_{\text{cn}} - E_{\text{cc}} + E_{\text{nc}} - E_{\text{nn}} \quad (4)$$

where E_{cn} is the energy of charged molecule (anion or cation) calculated using an optimal geometry of the neutral molecule, E_{nc} is the energy of the neutral molecule in the geometry optimized for charged molecule, and E_{nn} and E_{cc} are the energies of the neutral and charged molecules, respectively, taken at their corresponding optimal geometries. Transfer integrals are calculated by projecting the Fock matrix of the dimer (obtained from the experimental X-ray crystal geometry) onto molecular orbitals of the respective monomers²⁰ with the subsequent symmetric orthogonalization.⁶¹ The procedure is as

follows: by ab initio DFT we calculate the Fock matrix, \mathbf{F} , and the basis set overlap matrix, \mathbf{S} , for the dimer in the ground state. In addition, we calculate eigenvectors (molecular orbitals) for both monomers in their ground state: they are given as columns of the matrices \mathbf{T}_1 and \mathbf{T}_2 for the first and second monomers, respectively. Then we construct the block-diagonal matrix $\mathbf{B} = \text{diag}(\mathbf{T}_1, \mathbf{T}_2)$ and perform the projection: $\mathbf{F}' = \mathbf{B}^T \mathbf{F} \mathbf{B}$, $\mathbf{S}' = \mathbf{B}^T \mathbf{S} \mathbf{B}$. The elements of the matrices \mathbf{F}' and \mathbf{S}' corresponding to HOMO (LUMO) of both monomers compose the effective two-by-two Hamiltonian for holes (electrons), \mathbf{H} , and the overlap matrix \mathbf{O} . The transfer integral is the nondiagonal element of the matrix $\mathbf{O}^{-1/2} \mathbf{H} \mathbf{O}^{-1/2}$.

Finally, exciton diffusion length and charge carrier mobility are calculated by solving the Pauli kinetic equation for the crystal:¹⁹

$$\dot{p}_i(t) = -\tau^{-1} p_i(t) + \sum_j (p_j(t) w_{j \rightarrow i} - p_i(t) w_{i \rightarrow j}) \quad (5)$$

where $p_i(t)$ is the probability for the exciton or charge carrier to be localized on the i th molecule at the moment of time t , w are the calculated transfer rates, and τ is the exciton lifetime (for charges it is infinite). To evaluate the latter, we take the radiative lifetime calculated by the formula²⁶

$$\tau = \frac{3\hbar^4 c^3}{4E^3} |d|^2 \quad (6)$$

where E is the transition energy and d is the transition dipole moment. The explicit formulas expressing the diffusion tensor and diffusion length via transfer rates and crystal geometry are cumbersome and are given on p S12 of the Supporting Information. The mobility tensor, μ , is obtained from the diffusion tensor, D , by the Einstein relation $\mu = eD/(kT)$, where e is the electron charge.

To find the diffusion length we further calculate the mean square displacement tensor

$$\Lambda^{\alpha\beta} = \frac{1}{2\tau} \sum_i R_i^\alpha R_i^\beta \int_0^\infty p_i(t) dt \quad (7)$$

where R_i is the vector in Cartesian coordinates of the i th molecule, provided that initially the exciton was located at the origin. The square root of the trace of Λ gives the exciton diffusion length. Since $\Lambda \sim \tau D$ as $\tau \rightarrow \infty$, our definition of the diffusion length is consistent with the commonly used⁶² formula $(\tau D)^{1/2}$. Because the diffusion is anisotropic, it is more informative to calculate the square root of the eigenvalues of Λ , which gives the exciton diffusion length along the main axes of the tensor Λ . Note that in Monte Carlo simulations mean absolute displacement is usually calculated.²³

The comparison of various ab initio and semiempirical methods within different computational methodologies and the analysis of the assumed approximations have been performed as well and will be presented in subsequent publications.

III. RESULTS AND DISCUSSION

Molecular Geometry. The *p*-DTS(PTTh₂)₂ molecule, shown in Figure 1, consists of a π -conjugated backbone comprising a central electron-rich dithieno(3,2-b;2',3'-d)silole (DTS) moiety, adjacent [1,2,5]thiadiazolo[3,4-c]pyridine (PT) heterocycles, and terminal hexyl-substituted thiophene units. Single crystals suitable for X-ray diffraction studies were grown by slow vapor diffusion of acetone into a dichloromethane solution at 4 °C. A view of the resulting molecular structure is

shown in Figure 2. Note that, because the 2-ethylhexyl chains exist as superimposed R/S isomers, the anisotropic displace-

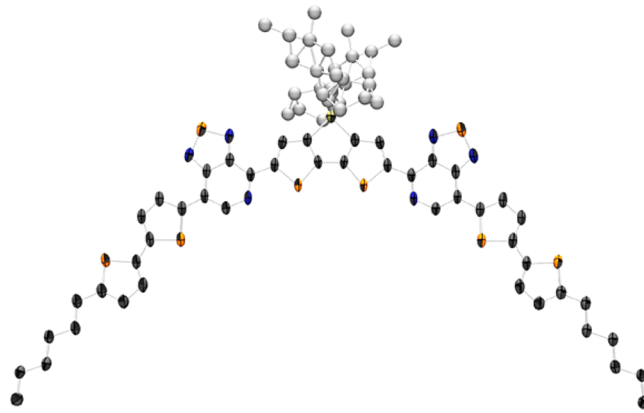


Figure 2. Molecular structure of *p*-DTS(PTTh₂)₂, as determined by a single-crystal X-ray diffraction study (ORTEP depiction at 50% probability). C, dark gray; Si, yellow; S, orange; N, blue; disordered carbons depicted in lighter gray; H, not shown.

ment parameters for the carbons could not be determined from the X-ray data. Therefore, the chains were modeled using constrained geometric parameters and isotropic temperature factors as follows: the R and S fragments were modeled by constraining the C–C and C–Si bond lengths and temperature factors to be the same for each fragment, with optimized occupancy being near equal. From Figure 2, one observes that *p*-DTS(PTTh₂)₂ adopts a distinctive curved shape, as opposed to a more linear geometry.⁶³ A measure of this departure from linearity can be obtained by noting that the angle between the Si bridgehead atom and the centroids in the terminal thiophene rings is 103.9°.

In the crystal *p*-DTS(PTTh₂)₂ forms stacks, as shown in Figure 3a, in which the orientation of the molecules alternates down the direction of the stacks. The π – π distance is approximately 3.5 Å within the stack (measured as the distance between the average planes of the molecules), with a slip-stack arrangement between the two molecules. When viewed along the stacking directions one observes a two-dimensional close-packed lattice as shown in Figure 3b and schematically cartooned in Figure 6a.

To test the computational methods and elucidate the influence of the molecular environment, we compare experimental (crystal) and computed (in vacuo and in solution) geometries of the conjugated framework. The mean square deviation is 0.01 Å for bond lengths, and 0.08° for bond angles. The global structure of the conjugated framework is compared using the “nonplanarity” parameter, which is the mean square deviation of the distances to the plane that minimizes this deviation (least-squares plane or orthogonal distance regression plane). For the optimized geometry the value of the nonplanarity is 0.19 Å in vacuo and 0.20 Å in chloroform with $\epsilon = 4.7$. In the experimental X-ray crystal geometry, this value is 0.05 Å. The difference shows that the molecules are more planar within the crystal lattice due to the π -stacking. These features are relevant for the observed red shifts in the absorption spectrum when transitioning from solution to the solid state.⁶⁴ Note also that, because of the shorter conjugation length, this effect is expected to be smaller than in conjugated

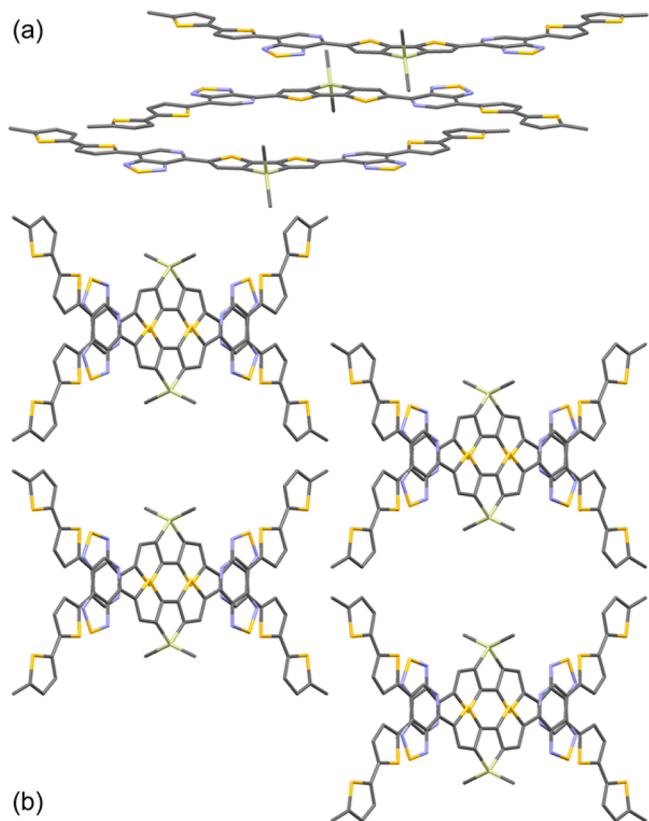


Figure 3. (a) Side view of the π -stack in the crystal. Hydrogens and aliphatic chains are not shown. The stacking period is two molecules. (b) The crystal viewed along the stacking direction. C, dark gray; Si, light green; S, yellow; N, blue; H, not shown.

polymers, e.g., various forms of polythiophene for both crystal versus solution⁶⁵ and regioregular versus regiorandom forms.⁶⁶

Electronic Structure and Analysis of UV–Vis Spectra in Solution. For the analysis of electronic excitations and carrier transport, three molecular orbitals (MOs) are essential: HOMO, LUMO, and LUMO + 1. The energy splitting of the latter two orbitals is 0.3 eV. The rest of the MOs lie about 0.4 eV below and 1 eV above these three. The HOMO is delocalized over the entire conjugated framework, except for the five-membered rings of the PT units, see Figure 4a. Two LUMOs show localization mainly on the two PT units. Electronic structure of a single molecule does not differ significantly for the geometries considered: as-in-crystal, optimized in *vacuo*, or optimized in solution (see Figure S1 of the Supporting Information).

The calculated UV–vis absorption spectra are shown in Figure 5 together with the experimental absorption and emission spectra taken in chloroform solution. The overall agreement between experimental and calculated absorption spectra is very good. The lowest optically active band gap transition is polarized along the long axis of the molecule. Our calculations interpret a shoulder on the blue side of the fundamental absorption peak as a second electronic transition (vs conventional assignment of this shoulder to vibronic transitions). Its transition dipole moment is perpendicular to the long axis of the molecule and, thus, is much smaller than the first state transition dipole moment because of the short extent of the wave function in this direction (see Table 1 and the discussion below). Finally, we assign the broad high-energy peak in the 3–4 eV range to multiple electronic transitions. Individual excited states can be further analyzed using natural transition orbitals (NTOs),^{67,68} which give a simple orbital picture of the results of TDDFT calculations, see Table 1. In

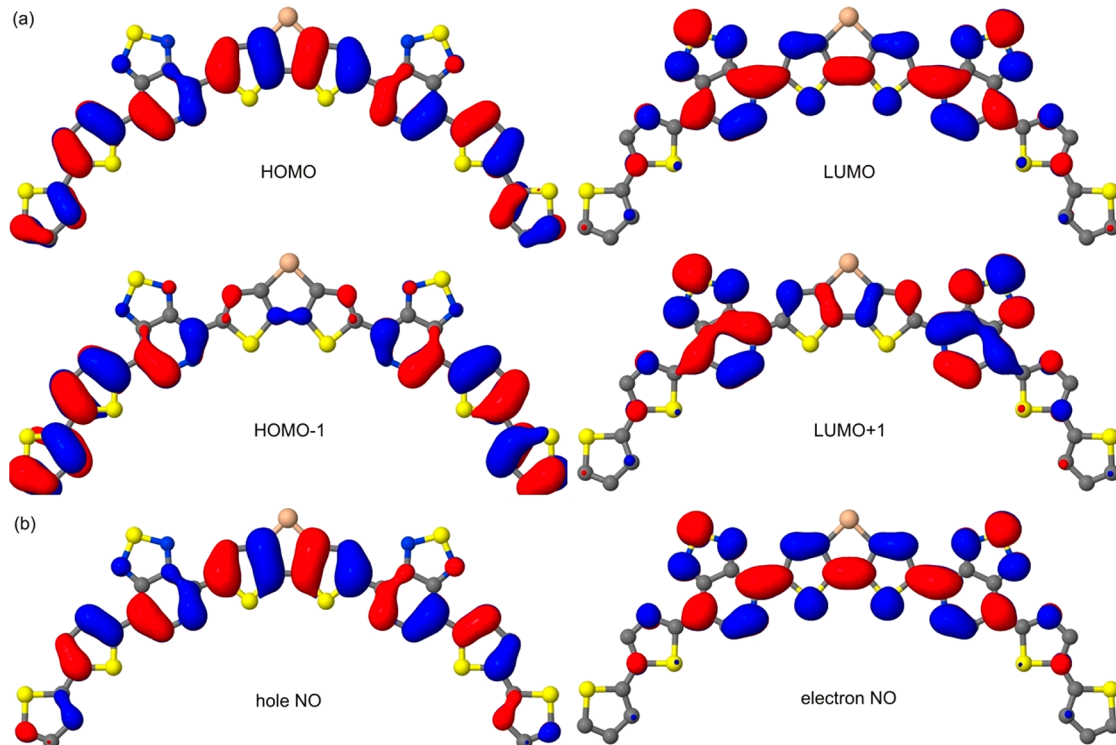


Figure 4. (a) Frontier molecular orbitals of *p*-DTS(PTTh₂)₂. Hydrogens and aliphatic chains are not shown. (b) Half-filled natural orbitals for electron and hole polarons, obtained for optimized anion and cation species.

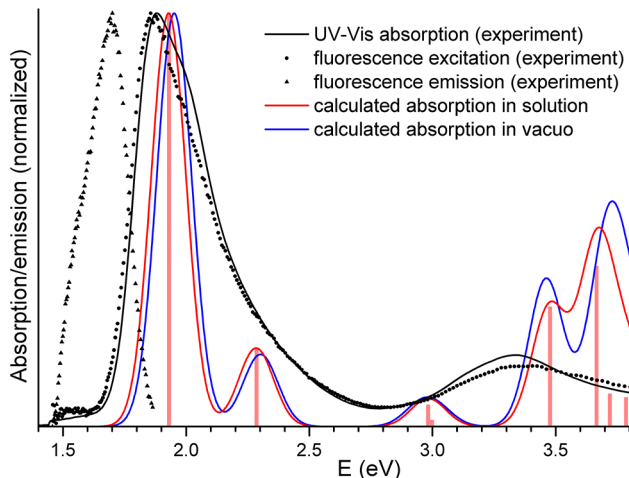


Figure 5. Emission and absorption spectra of *p*-DTS(PTTh₂)₂ molecule. Experimental spectra are obtained in chloroform solution. Calculated spectral lines (CAM-B3LYP/6-31G) are broadened by a Gaussian function with a line width of 0.05 eV. Individual transitions are shown by bars whose heights are proportional to the oscillator strengths of the transitions.

this analysis each electronic transition is represented in terms of two orbitals (electron and hole).

Now we focus our discussion on the first two transitions constituting the lowest-energy absorption band in the experimental spectrum (Figure 5). By comparing the hole and electron NTOs in Table 1 with HOMOs and LUMOs in Figure 4a we see that the first transition is essentially HOMO–LUMO transition and the second transition is HOMO–LUMO + 1 transition. The small difference between the hole NTO and the HOMO is due to a slight hole localization that is expected for such sufficiently long conjugated molecule. LUMOs are largely localized on the PT units; therefore, no further localization for the electron NTO is expected except possible symmetry breaking with complete electron localization on one PT unit. Both transitions have partial charge-transfer character with the PT unit acting as an acceptor for given optical transitions from the ground to excited states. A similar picture applies to NTOs describing higher excited states: every optical transition leads to a partial electron transfer from the peripheral rings or the central DTS unit to the two PT groups, in accordance to common chemical intuition.

The polarization of electronic transition using the orbital picture can be rationalized as follows. First, note that the conjugated frameworks themselves have an approximate C_{2v} symmetry; the HOMO and two LUMOs have approximate a_2 , b_1 , and a_2 symmetries, respectively (a_2 is c_2 symmetry and b_1 is σ_{perp} symmetry). According to this approximate symmetry, the transition dipole for the HOMO–LUMO transition is oriented along the conjugated framework (b_2 symmetry), while the dipole for the HOMO–LUMO + 1 transition is oriented perpendicular to the molecular long axis (a_1 symmetry). The rest of the MOs are relatively isolated. Therefore, we expect to see an isolated absorption peak composed of the lowest-energy strong HOMO–LUMO and the higher-energy weak HOMO–LUMO + 1 transitions in the polarization spectroscopy of aligned samples.

Analysis of Fluorescence Excitation/Emission Spectra.

To estimate the spectral overlap and other parameters of the exciton transport we analyze the shape of the emission and first

absorption bands determined by the fluorescence spectroscopy (Figure 5). To fit the experimental spectra, we assume the displaced harmonic oscillator model, consistent with the results of ab initio calculations (see Figures S2 and S3 of the Supporting Information). The spectral shape of the first absorption band in Figure 5 is formed by the vibrational broadening of the two electronic transitions. Each vibronic transition is further broadened mainly by external factors such as inhomogeneous broadening. We assume that this broadening is small compared to the vibronic progression, and describe it by the Gaussian function, so that each vibronic transition has Gaussian line shape with the same dispersion σ .

The spectra of large molecules are vibrationally broadened well enough so that their 0–0 edge can be approximated by the Gaussian shape:

$$\rho(E) = \frac{1}{\sqrt{2\pi(2\lambda'kT + \sigma^2)}} \times \exp\left(-\frac{(E - E_{00} \pm \lambda')^2}{4\lambda'kT + 2\sigma^2} - S''\right) \quad (8)$$

Here λ' is the effective reorganization energy due to the environment and classic intramolecular vibrational modes (whose energy is much smaller than the temperature), S'' is the effective Huang–Rhys factor for the “quantum” vibrational modes (collective coordinate for the rest of the modes), σ is an inhomogeneous line broadening, E_{00} is 0–0 transition energy, the upper sign at λ' is for emission, and the lower one is for absorption. This formula is detailed on p S2 of the Supporting Information and corresponds to the 0–0 transition description in the Bixon and Jortner model.^{19,69} The results of the experimental spectra fits and cross-checks (see Figure S5 and Table S3 of the Supporting Information) show that the chosen model is adequate, and the fitting parameters are $\lambda'_{\text{abs}} = 0.11$ eV, $\lambda'_{\text{emi}} = 0.07$ eV, $S''_{\text{abs}} = 0.4$, $S''_{\text{emi}} = 0.2$, $\sigma = 0.04$ eV, $E_{00} = 1.75$ eV. The inhomogeneous broadening is small compared to $(2\lambda'kT)^{1/2} = 0.1$ eV; therefore, the experimental line shapes can be used for the spectral overlap estimate.

The spectral overlap, J , is calculated as follows: the lower estimate is obtained by using the Gaussian shape (formula 8) with the above-determined parameters but no inhomogeneous broadening ($\sigma = 0$). The upper estimate is obtained with $\sigma = 0.04$ eV, assuming that the inhomogeneous broadenings of individual molecules are independent. This gives a calculated J of 0.4–0.6 eV⁻¹, and the direct convolution of the measured spectra gives a value, 0.6 eV⁻¹, similar to the calculated upper bound value. When using the obtained spectral overlap value for calculating exciton-transfer rates in the crystal, we assume that the spectral broadening in the crystal is not larger than in the solution.

To determine the exciton transport regime we need to evaluate the corresponding reorganization energy, which can be estimated by the formula

$$\lambda = \lambda'_{\text{emi}} + \lambda'_{\text{abs}} + (S''_{\text{emi}} + S''_{\text{abs}})\hbar\omega'' \quad (9)$$

where ω'' is the effective frequency for the quantum modes. The latter are typically C=C stretching modes^{27,70} with $\hbar\omega'' \sim 0.2$ eV; hence, $\lambda = 0.3$ eV. The alternative estimate based on the global analysis of the spectra (formula S5 of the Supporting Information) gives the same value.

Exciton Transport. From the crystal structure in Figure 3b, one can build a simplified picture of how the stacks organize

Table 1. Natural Transitions Orbitals for the First Five Excited States of the Molecule in Chloroform Obtained from TD-CAM-B3LYP/6-31G Calculations^a

parameters	hole NTO		electron NTO
E = 1.94 eV f = 1.83 NTO w = 0.84 CI w = 0.40 HOMO-> LUMO			
E = 2.29 eV f = 0.35 NTO w = 0.61 CI w = 0.30 HOMO-> LUMO+1			
E = 2.99 eV f = 0.10 NTO w = 0.50 CI w = 0.24 HOMO+HOMO-2 ->LUMO+1			
E = 3.00 eV f = 0.03 NTO w = 0.56 CI w = 0.25 HOMO-2-> LUMO			
E = 3.49 eV f = 0.54 NTO w = 0.53 CI w = 0.25 HOMO-> LUMO+2			

^aNotations: “E” is the transition energy, “f” is the respective oscillator strength, “NTO w” is the weight of the given NTO pair in the corresponding transition density matrix, “CI w” is the weight of the Kohn–Sham orbital pair in the corresponding transition density matrix. The latter two molecular orbitals are identified in the following two lines.

themselves, as shown in the cartoon representation in Figure 6a. A map depicting the largest intermolecular exciton couplings is shown in Figure 6b. Because excitons can move via the long-range Förster transfer mechanism, their transport does not depend strongly on the local intermolecular structure. As a result, we see in Figure 6b a more or less isotropic distribution of couplings. The strongest coupling, 63 meV (500 cm⁻¹), is between the nearest neighbors in the π -stack. At large intermolecular separations compared to the monomer’s size we expect to observe an inverse cubic dependence of couplings on the distance between the monomers due to a dipole–dipole type of interaction. In fact, even for hundreds of dimers we

calculate (all dimers within a given maximum 30 Å contact distance) the observed distance dependence is much smaller (Supporting Information Figure S7). This is because the molecules are large, 26 Å without aliphatic chains, and of complex shape.⁷¹ This justifies our approach to evaluate excitonic couplings from the splitting of excited states in a dimer, compared to a less accurate point–dipole approximation. In comparison to other organic conjugated systems, our estimated absolute values of the couplings are moderate: couplings exceeding 100 meV are not rare.^{22,26,57}

The above-calculated couplings should be corrected for the effects of the crystalline environment.⁷¹ At large intermolecular

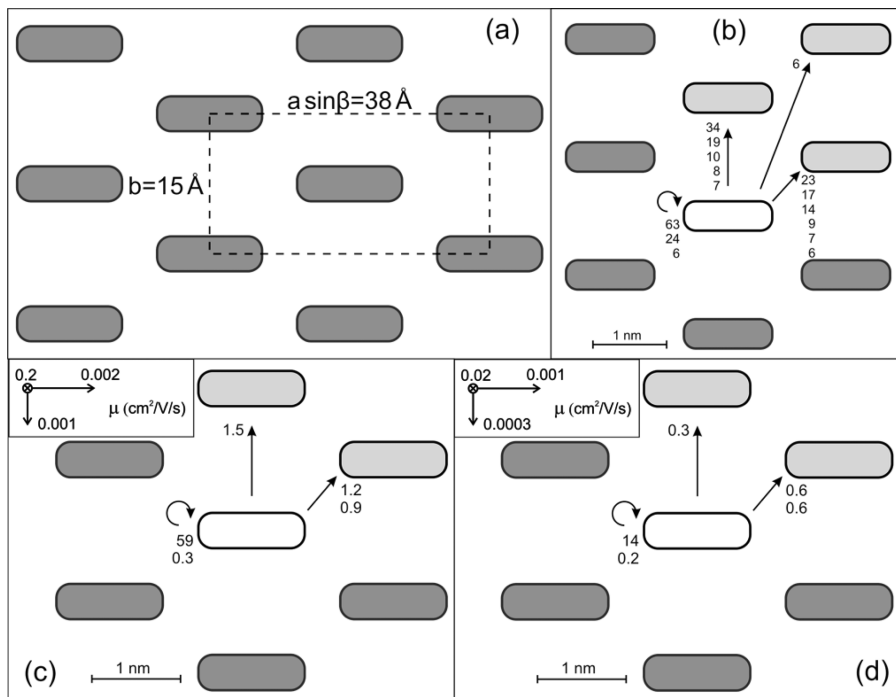


Figure 6. (a) Cartoon version of Figure 3b summarizing the important features of the crystal lattice. Here π -stacks run perpendicular to the figure plane and are represented as the rounded rectangles. The on-plane projection of the monoclinic unit cell is shown as the dashed rectangle. The stacking direction is along the c -axis. (b) Excitonic intermolecular couplings (absolute values in meV) are shown for all dimers coupled stronger than 5 meV. All molecules are equivalent. Some dimers are also equivalent: the dark gray rectangles (π -stacks) are symmetry-equivalent to the light gray ones. The circled arrow denotes the intrastack couplings, e.g., 63 meV is for the nearest neighbors in the π -stack, 24 meV is for the next nearest neighbors, etc. Similarly, there is a number of interstack dimers for each pair of stacks (the straight arrows); the corresponding couplings are listed in the descending order. (c) Hole-transfer integrals (meV) shown for all dimers coupled stronger than 0.1 meV. The calculated hole mobilities along the main axes of the mobility tensor are shown in the inset. (d) Same as panel c but for electrons.

distances, these effects reduce the couplings by the squared refraction index of the crystal. Unfortunately the crystal absorbs light at the frequencies of interest, severely complicating the estimation of this index. At small distances the effects are even more complicated,⁷¹ though the ab initio calculations for small multimers (Table S4 of the Supporting Information) show that the dimer-in-vacuo approximation gives correct couplings for these systems.

Because the largest excitonic coupling, 63 meV, is much smaller than our evaluated internal reorganization energy, $\lambda = 0.3$ eV, we expect that relaxed excitons will move via the hopping mechanism.²² The calculated largest intermolecular transfer rate, $1/60 \text{ fs}^{-1}$, is comparable with intramolecular relaxation rates,^{72,73} implying that the hopping is not purely incoherent. More accurate analysis of the transport regime is given on pp S10–S11 of the Supporting Information. The estimated by formula 6 exciton radiative lifetime is 2.5 ns.

The calculated exciton diffusion length of about 100–400 nm depends on the direction of diffusion in the crystal, with the largest diffusion length being along the π -stack. Note that this estimate is valid only for an idealized crystal. In fact, nonradiative processes and traps decrease the exciton diffusion length substantially.⁶² However, if the concentration of defects (except for the grain boundaries) is low enough to have a majority of crystallites free of deep traps, we can state that the relaxed excitons are able to sample the entire crystallite because the typical crystallite size in thin films, 20–30 nm,⁴⁷ is much smaller than the estimated exciton diffusion length. Practically, this means that photogenerated excitons can be delivered to the charge-separating interface with 100% efficiency for trap-free

crystallites. This is true if the crystallites are surrounded by fullerene within the BHJ blend, which may or may not be the case in a real device layer.

Charge Carrier Transport. Maps of the intermolecular transfer integrals for holes and electrons are shown in Figure 6, parts c and d, respectively. Because transfer integrals depend exponentially on the contact distance between the underlying conjugated bases, they are essentially nonzero only for the nearest neighbor molecules. Transfer integrals between the π -stacked molecules are 1–2 orders of magnitude larger than those for other dimers. Therefore, the transport of charge carriers occurs mainly along the π -stack.

The calculated internal reorganization energies are 0.43 and 0.36 eV for the hole and electron polarons, respectively, implying that we are in the regime of strong electron–phonon coupling and the small-polaron hopping model is the correct approximation. The natural orbitals (NO) obtained for the cation and anion species are shown in Figure 4b: the electron NO coincides with the LUMO, whereas the hole NO is slightly more localized compared to the HOMO. We have observed the same picture for the NTO analysis of the excitonic transition. Comparison of calculated NOs and HOMO/LUMO justifies our assumption of the latter being states of electron and hole on a single molecule, central to the charge transport calculations.

Calculated transfer rates between π -stacked molecules are 1.6 ps^{-1} for holes and 0.2 ps^{-1} for electrons. These values are slower than intramolecular relaxation rates for charges. The largest transfer rates across the stack are 2–3 orders of magnitude smaller.

The calculated hole mobility along the π -stack is $0.2 \text{ cm}^2/\text{V}\cdot\text{s}$. This value is 2 orders of magnitude smaller than the highest experimentally reported mobility for molecular crystals²¹ (e.g., pentacene). However, this single-crystal mobility is about 2 orders of magnitude larger than the measured mobility in thin films of optimized *p*-DTS(PTTh₂)₂/PC₇₀BM blends.⁴⁷ For the pristine *p*-DTS(PTTh₂)₂ thin films cast from a solution the measured hole mobility in the saturation regime is $0.1 \text{ cm}^2/\text{V}\cdot\text{s}$.⁴⁷ A crude estimate of this high-field mobility for a crystal can be obtained by omitting the exponent in formula 3. Thus calculated value is again 2 orders of magnitude larger than the measured thin film mobility. In contrast to excitons, we expect that holes are efficiently transported through the crystallites only along the π -stacks (in the absence of any traps).

In the crystal the effects of thermal disorder should not influence hole transport along the π -stack due to the delocalization of the HOMO over the conjugated framework combined with the large intermolecular contact area. LUMO states are localized on PT units; therefore, the thermal disorder is expected to suppress electron mobility. Across the stack transport proceeds via point contacts; therefore, those transfer integrals must be thermally averaged.⁷⁴

Finally, we can compare the calculated ionization potential (IP) and electron affinity (EA) with those determined by cyclic voltammetry.⁴⁷ The definitions of these quantities are uncertain to the amount of the geometry relaxation energy (i.e., whether the neutral or charged states are vibronically relaxed or not).⁷⁵ Also the results of cyclic voltammetry measurements are influenced by the details of the process, in particular by interfacial dipole built up on the electrodes, solvent effects, and possibly the vicinity of charge compensation ions.⁷⁶ The adiabatic limit, i.e., $\text{IP} = E_{\text{cation}} - E_{\text{ground}}$ and $\text{EA} = E_{\text{ground}} - E_{\text{anion}}$ with fully relaxed geometries, seems to be more appropriate for "slow" cyclic voltammetry. In the usually plotted energy-level diagrams, "HOMO" and "LUMO" levels correspond to $-\text{IP}$ and $-\text{EA}$ values, respectively. The calculated IP, 5.3 eV (in solution), is in agreement with the cyclic voltammetry estimate, 5.2 eV. The calculated EA is 2.9 eV, whereas the cyclic voltammetry estimate is 3.6 eV; the difference is within the uncertainty limits of the latter method⁷⁷ (the measured reduction onset referenced to Fc/Fc⁺ is -1.3 V). Note that in the opposite, fixed geometry limit, IP = 5.5 eV and EA = 2.7 eV.

IV. CONCLUSIONS

In summary, the electronic properties of *p*-DTS(PTTh₂)₂ in a variety of environments were investigated using DFT approach. Of particular relevance to the function of OPVs is that the structural information is obtained from X-ray diffraction studies of crystals similar to those observed in the donor domains of high-efficiency OPVs. It is difficult to anticipate obtaining such structural details with the more widely used conjugated polymer donor materials due to their higher amorphous content and inability to obtain suitable single crystals. Our DFT and TD-DFT calculations show that at the molecular level the electrons in *p*-DTS(PTTh₂)₂ are mostly localized on the two central PT units, and we observe that the LUMO, electron NTO, and electron NO are visually identical. The HOMO is delocalized over the entire chromophore, and we observe some localization of exciton and hole polaron such that hole NTO and hole NO are visually identical.

The first absorption peak corresponds to a HOMO–LUMO transition with the transition dipole oriented along the long axis

of the conjugated framework. Exciton transport is nearly isotropic in the crystal. The calculated diffusion length of the excitons exceeds the typical size of crystallites experimentally observed in the OPV devices. Hole transport occurs mainly through the π -stacks with a moderate computed mobility. The transport along the stack is not influenced by the thermal disorder due to the large intermolecular contact area. Therefore, we can conclude that there is no "power conversion efficiency loss" on the scale of a single crystallite, provided that it is surrounded by the fullerene phase. We recognize that the reality in a real BHJ active layer is different; for example, there may be amorphous domains of *p*-DTS(PTTh₂)₂ or incompletely phase-separated domains. These imperfections may account for the losses in efficiency because of their influence on charge separation process⁷⁸ and charge transport on a mesoscale, for example, because of grain boundaries, interfaces, and incomplete percolation pathways.

Overall, our investigation shows that the high power conversion efficiency of *p*-DTS(PTTh₂)₂ is not due to a "special" electronic feature, but rather due to a combination of multiple properties, including broad UV–vis light absorption, the combination of several donor- and acceptor-rich components on a single molecule giving rise to charge-transfer characteristics and efficient intermolecular charge transport, ability to form crystallites of the correct size, the ease of achieving high levels of chemical purity, and the optimized morphology of the active layer. A few concluding remarks can be made within the context of designing new small-molecule donors for improving the solar cell efficiency. Larger conjugated backbones lead to lower energy absorption and higher molar extinction coefficients. Crystalline domains allow for exciton "delocalization" and additional red-shifts of optical absorption spectra. It is also reasonable that larger intrastack contact area makes the charge transport more disorder-resistant. Smaller intrastack separation would conversely increase the hole-transfer integrals between the π -conjugated stacks. Tightly packed stack geometry suppresses molecule buckling and, as result, increases the spectral overlap for excitons and decreases the reorganization energy for holes.

In the current contribution we focus on the transport properties in the crystalline domains of a small molecule, since it has been experimentally observed that these small-molecule domains dominate thin films in OPV devices. Recent theoretical work has attempted to evaluate the effects of conformational disorder for frontier orbital delocalization and for charge/exciton delocalization and transport.^{30,79} We will use similar methodologies to assess the impact of interfaces between crystalline grains and amorphous regions on the transport and photovoltaic device performance in future studies.

ASSOCIATED CONTENT

S Supporting Information

Plots of molecular orbitals, details on displaced harmonic oscillator model, ab initio calculations for spectra, analysis of experimental spectra, details on exciton couplings, analysis of exciton transport regime, solution of kinetic equation, crystal synthesis, and structural characterization including the cif file. This material is available free of charge via the Internet at <http://pubs.acs.org>.

AUTHOR INFORMATION

Corresponding Author

*E-mail: serg@lanl.gov (S.T.); bazan@chem.ucsb.edu (G.C.B.).

Notes

The authors declare no competing financial interest.

ACKNOWLEDGMENTS

A.Z. thanks Enrique Batista for helpful suggestions on computational methodology and Stavros Athanasopoulos for discussions on disorder effects. We acknowledge support for the synthesis of the materials and calculation efforts the Center for Energy Efficient Materials (CEEM), an Energy Frontier Research Center funded by the U.S. Department of Energy (DOE), Office of Basic Energy Sciences (BES). We also acknowledge support of the Los Alamos Laboratory Directed Research and Development program. Los Alamos National Laboratory (LANL) is operated by Los Alamos National Security, LLC, for the National Nuclear Security Administration of the U.S. Department of Energy under contract DE-AC52-06NA25396. We acknowledge support of the Center for Integrated Nanotechnology (CINT) and Center for Nonlinear Studies (CNLS) at LANL. This material is based upon work supported by the National Science Foundation under CHE-1040541.

ABBREVIATIONS

BHJ, bulk heterojunction; CI, configuration interaction; DFT, density functional theory; HOMO, highest occupied molecular orbital; LUMO, lowest unoccupied molecular orbital; MO, molecular orbital; NO, natural orbital; NTO, natural transition orbital; OPV, organic photovoltaic devices; TDDFT, time-dependent density functional theory

REFERENCES

- (1) Li, G.; Zhu, R.; Yang, Y. Polymer Solar Cells. *Nat. Photonics* **2012**, *6*, 153–161.
- (2) Service, R. F. Outlook Brightens for Plastic Solar Cells. *Science* **2011**, *332*, 293.
- (3) Heeger, A. J. Semiconducting Polymers: The Third Generation. *Chem. Soc. Rev.* **2010**, *39*, 2354–2371.
- (4) Kippelen, B.; Bredas, J.-L. Organic Photovoltaics. *Energy Environ. Sci.* **2009**, *2*, 251–261.
- (5) *Organic Photovoltaics: Materials, Device Physics, and Manufacturing Technologies*; Brabec, C. J., Dyakonov, V., Scherf, U., Eds.; Wiley-VCH: Weinheim, Germany, 2008.
- (6) Hoppe, H.; Sariciftci, N.; Marder, S.; Lee, K.-S., Eds.; *Advances in Polymer Science*; Springer: Berlin/Heidelberg, Germany: 2008; Vol. 214, pp 1–86.
- (7) Cheng, Y.-J.; Yang, S.-H.; Hsu, C.-S. Synthesis of Conjugated Polymers for Organic Solar Cell Applications. *Chem. Rev.* **2009**, *109*, 5868–5923.
- (8) Günes, S.; Neugebauer, H.; Sariciftci, N. S. Conjugated Polymer-Based Organic Solar Cells. *Chem. Rev.* **2007**, *107*, 1324–1338.
- (9) Chen, L.-M.; Hong, Z.; Li, G.; Yang, Y. Recent Progress in Polymer Solar Cells: Manipulation of Polymer:Fullerene Morphology and the Formation of Efficient Inverted Polymer Solar Cells. *Adv. Mater.* **2009**, *21*, 1434–1449.
- (10) Chen, J.; Cao, Y. Development of Novel Conjugated Donor Polymers for High-Efficiency Bulk-Heterojunction Photovoltaic Devices. *Acc. Chem. Res.* **2009**, *42*, 1709–1718.
- (11) Li, C.; Liu, M.; Pschirer, N. G.; Baumgarten, M.; Müllen, K. Polyphenylene-Based Materials for Organic Photovoltaics. *Chem. Rev.* **2010**, *110*, 6817–6855.
- (12) Brabec, C. J.; Gowrisankar, S.; Halls, J. J. M.; Laird, D.; Jia, S.; Williams, S. P. Polymer–Fullerene Bulk-Heterojunction Solar Cells. *Adv. Mater.* **2010**, *22*, 3839–3856.
- (13) Inganäs, O.; Zhang, F.; Tvingstedt, K.; Andersson, L. M.; Hellström, S.; Andersson, M. R. Polymer Photovoltaics with Alternating Copolymer/Fullerene Blends and Novel Device Architectures. *Adv. Mater.* **2010**, *22*, E100–E116.
- (14) Beaujuge, P. M.; Fréchet, J. M. J. Molecular Design and Ordering Effects in π -Functional Materials for Transistor and Solar Cell Applications. *J. Am. Chem. Soc.* **2011**, *133*, 20009–20029.
- (15) Servaites, J. D.; Ratner, M. A.; Marks, T. J. Organic Solar Cells: A New Look at Traditional Models. *Energy Environ. Sci.* **2011**, *4*, 4410–4422.
- (16) Dennler, G.; Scharber, M. C.; Brabec, C. J. Polymer–Fullerene Bulk-Heterojunction Solar Cells. *Adv. Mater.* **2009**, *21*, 1323–1338.
- (17) Brédas, J.-L.; Norton, J. E.; Cornil, J.; Coropceanu, V. Molecular Understanding of Organic Solar Cells: The Challenges. *Acc. Chem. Res.* **2009**, *42*, 1691–1699.
- (18) Coropceanu, V.; Cornil, J.; da Silva Filho, D. A.; Olivier, Y.; Silbey, R.; Brédas, J.-L. Charge Transport in Organic Semiconductors. *Chem. Rev.* **2007**, *107*, 926–952.
- (19) Brédas, J.-L.; Beljonne, D.; Coropceanu, V.; Cornil, J. Charge-Transfer and Energy-Transfer Processes in π -Conjugated Oligomers and Polymers: A Molecular Picture. *Chem. Rev.* **2004**, *104*, 4971–5004.
- (20) Shuai, Z.; Wang, L.; Li, Q. Evaluation of Charge Mobility in Organic Materials: From Localized to Delocalized Descriptions at a First-Principles Level. *Adv. Mater.* **2011**, *23*, 1145–1153.
- (21) Grozema, F. C.; Siebbeles, L. D. A. Mechanism of Charge Transport in Self-Organizing Organic Materials. *Int. Rev. Phys. Chem.* **2008**, *27*, 87–138.
- (22) Troisi, A. Charge Transport in High Mobility Molecular Semiconductors: Classical Models and New Theories. *Chem. Soc. Rev.* **2011**, *40*, 2347–2358.
- (23) Papadopoulos, T. A.; Muccioli, L.; Athanasopoulos, S.; Walker, A. B.; Zannoni, C.; Beljonne, D. Does Supramolecular Ordering Influence Exciton Transport in Conjugated Systems? Insight From Atomistic Simulations. *Chem. Sci.* **2011**, *2*, 1025–1032.
- (24) Lukyanov, A.; Andrienko, D. Extracting Nondispersive Charge Carrier Mobilities of Organic Semiconductors from Simulations of Small Systems. *Phys. Rev. B* **2010**, *82*, 193202.
- (25) Athanasopoulos, S.; Kirkpatrick, J.; Martínez, D.; Frost, J. M.; Foden, C. M.; Walker, A. B.; Nelson, J. Predictive Study of Charge Transport in Disordered Semiconducting Polymers. *Nano Lett.* **2007**, *7*, 1785–1788.
- (26) Hennebicq, E.; Pourtois, G.; Scholes, G. D.; Herz, L. M.; Russell, D. M.; Silva, C.; Setayesh, S.; Grimsdale, A. C.; Müllen, K.; Brédas, J.-L.; et al. Exciton Migration in Rigid-Rod Conjugated Polymers: An Improved Förster Model. *J. Am. Chem. Soc.* **2005**, *127*, 4744–4762.
- (27) Karabunarliev, S.; Baumgarten, M.; Bittner, E. R.; Müllen, K. Rigorous Franck–Condon Absorption and Emission Spectra of Conjugated Oligomers from Quantum Chemistry. *J. Chem. Phys.* **2000**, *113*, 11372–11381.
- (28) Risko, C.; McGehee, M. D.; Bredas, J.-L. A Quantum-Chemical Perspective into Low Optical-Gap Polymers for Highly-Efficient Organic Solar Cells. *Chem. Sci.* **2011**, *2*, 1200–1218.
- (29) Emelianova, E. V.; Athanasopoulos, S.; Silbey, R. J.; Beljonne, D. 2D Excitons as Primary Energy Carriers in Organic Crystals: The Case of Oligoacenes. *Phys. Rev. Lett.* **2010**, *104*, 206405.
- (30) Kilina, S.; Batista, E. R.; Yang, P.; Tretiak, S.; Saxena, A.; Martin, R. L.; Smith, D. L. Electronic Structure of Self-Assembled Amorphous Polyfluorenes. *ACS Nano* **2008**, *2*, 1381–1388.
- (31) Tretiak, S.; Igumenshchev, K.; Chernyak, V. Exciton Sizes of Conducting Polymers Predicted by Time-Dependent Density Functional Theory. *Phys. Rev. B* **2005**, *71*, 033201.
- (32) Igumenshchev, K. I.; Tretiak, S.; Chernyak, V. Y. Excitonic Effects in a Time-Dependent Density Functional Theory. *J. Chem. Phys.* **2007**, *127*, 114902–114910.

- (33) Magyar, R. J.; Tretiak, S. Dependence of Spurious Charge-Transfer Excited States on Orbital Exchange in TDDFT: Large Molecules and Clusters. *J. Chem. Theory Comput.* **2007**, *3*, 976–987.
- (34) Peach, M. J. G.; Cohen, A. J.; Tozer, D. J. Influence of Coulomb-Attenuation on Exchange-Correlation Functional Quality. *Phys. Chem. Chem. Phys.* **2006**, *8*, 4543–4549.
- (35) Peach, M. J. G.; Benfield, P.; Helgaker, T.; Tozer, D. J. Excitation Energies in Density Functional Theory: An Evaluation and a Diagnostic Test. *J. Chem. Phys.* **2008**, *128*, 044118–044118.
- (36) Karabunarliev, S.; Bittner, E. R.; Baumgarten, M. Franck-Condon Spectra and Electron-Libration Coupling in Para-polyphenyls. *J. Chem. Phys.* **2001**, *114*, 5863–5870.
- (37) Tretiak, S.; Saxena, A.; Martin, R. L.; Bishop, A. R. Conformational Dynamics of Photoexcited Conjugated Molecules. *Phys. Rev. Lett.* **2002**, *89*, 097402.
- (38) Nayyar, I. H.; Batista, E. R.; Tretiak, S.; Saxena, A.; Smith, D. L.; Martin, R. L. Localization of Electronic Excitations in Conjugated Polymers Studied by DFT. *J. Phys. Chem. Lett.* **2011**, *2*, 566–571.
- (39) Scharber, M. C.; Mühlbacher, D.; Koppe, M.; Denk, P.; Waldauf, C.; Heeger, A. J.; Brabec, C. J. Design Rules for Donors in Bulk-Heterojunction Solar Cells—Towards 10% Energy-Conversion Efficiency. *Adv. Mater.* **2006**, *18*, 789–794.
- (40) Liang, Y.; Xu, Z.; Xia, J.; Tsai, S.-T.; Wu, Y.; Li, G.; Ray, C.; Yu, L. For the Bright Future—Bulk Heterojunction Polymer Solar Cells with Power Conversion Efficiency of 7.4%. *Adv. Mater.* **2010**, *22*, E135–E138.
- (41) Gendron, D.; Leclerc, M. New Conjugated Polymers for Plastic Solar Cells. *Energy Environ. Sci.* **2011**, *4*, 1225–1237.
- (42) Roncali, J. Molecular Bulk Heterojunctions: An Emerging Approach to Organic Solar Cells. *Acc. Chem. Res.* **2009**, *42*, 1719–1730.
- (43) Mishra, A.; Bäuerle, P. Small Molecule Organic Semiconductors on the Move: Promises for Future Solar Energy Technology. *Angew. Chem., Int. Ed.* **2012**, *51*, 2020–2067.
- (44) Lin, Y.; Li, Y.; Zhan, X. Small Molecule Semiconductors for High-Efficiency Organic Photovoltaics. *Chem. Soc. Rev.* **2012**, *41*, 4245–4272.
- (45) Walker, B.; Kim, C.; Nguyen, T.-Q. Small Molecule Solution-Processed Bulk Heterojunction Solar Cells. *Chem. Mater.* **2011**, *23*, 470–482.
- (46) Welch, G. C.; Perez, L. A.; Hoven, C. V.; Zhang, Y.; Dang, X.-D.; Sharenko, A.; Toney, M. F.; Kramer, E. J.; Nguyen, T.-Q.; Bazan, G. C. A Modular Molecular Framework for Utility in Small-Molecule Solution-Processed Organic Photovoltaic Devices. *J. Mater. Chem.* **2011**, *21*, 12700–12709.
- (47) Sun, Y.; Welch, G. C.; Leong, W. L.; Takacs, C. J.; Bazan, G. C.; Heeger, A. J. Solution-Processed Small-Molecule Solar Cells with 6.7% Efficiency. *Nat. Mater.* **2012**, *11*, 44–48.
- (48) Lloyd, M. T.; Anthony, J. E.; Malliaras, G. G. Photovoltaics From Soluble Small Molecules. *Mater. Today* **2007**, *10*, 34–41.
- (49) Frisch, M. J.; et al. *Gaussian 09*, revision A.1; Gaussian, Inc.: Wallingford, CT, 2009.
- (50) Yanai, T.; Tew, D. P.; Handy, N. C. A New Hybrid Exchange-Correlation Functional Using the Coulomb-Attenuating Method (CAM-B3LYP). *Chem. Phys. Lett.* **2004**, *393*, 51–57.
- (51) Franc, M. M.; Pietro, W. J.; Hehre, W. J.; Binkley, J. S.; Gordon, M. S.; DeFrees, D. J.; Pople, J. A. Self-Consistent Molecular Orbital Methods. XXIII. A Polarization-Type Basis Set for Second-Row Elements. *J. Chem. Phys.* **1982**, *77*, 3654–3665.
- (52) Takano, Y.; Houk, K. N. Benchmarking the Conductor-like Polarizable Continuum Model (CPCM) for Aqueous Solvation Free Energies of Neutral and Ionic Organic Molecules. *J. Chem. Theory Comput.* **2004**, *1*, 70–77.
- (53) Cossi, M.; Rega, N.; Scalmani, G.; Barone, V. Energies, Structures, and Electronic Properties of Molecules in Solution with the C-PCM Solvation Model. *J. Comput. Chem.* **2003**, *24*, 669–681.
- (54) Barone, V.; Cossi, M. Quantum Calculation of Molecular Energies and Energy Gradients in Solution by a Conductor Solvent Model. *J. Phys. Chem. A* **1998**, *102*, 1995–2001.
- (55) Davydov, A. S. *Theory of Molecular Excitons*; Plenum Press: New York, 1971.
- (56) Tretiak, S.; Middleton, C.; Chernyak, V.; Mukamel, S. Bacteriochlorophyll and Carotenoid Excitonic Couplings in the LH2 System of Purple Bacteria. *J. Phys. Chem. B* **2000**, *104*, 9540–9553.
- (57) Tretiak, S.; Middleton, C.; Chernyak, V.; Mukamel, S. Exciton Hamiltonian for the Bacteriochlorophyll System in the LH2 Antenna Complex of Purple Bacteria. *J. Phys. Chem. B* **2000**, *104*, 4519–4528.
- (58) Tretiak, S.; Zhang, W. M.; Chernyak, V.; Mukamel, S. Excitonic Couplings and Electronic Coherence in Bridged Naphthalene Dimers. *Proc. Natl. Acad. Sci. U.S.A.* **1999**, *96*, 13003–13008.
- (59) Vos, R.; Engelborghs, Y.; Izard, J.; Baty, D. Fluorescence Study of the Three Tryptophan Residues of the Pore-Forming Domain of Colicin A Using Multifrequency Phase Fluorometry. *Biochemistry* **1995**, *34*, 1734–1743.
- (60) Holzhey, A.; Uhrich, C.; Brier, E.; Reinhold, E.; Bauerle, P.; Leo, K.; Hoffmann, M. Exciton Diffusion and Energy Transfer in Organic Solar Cells Based on Dicyanovinyl-Terthiophene. *J. Appl. Phys.* **2008**, *104*, 064510.
- (61) Newton, M. D. Quantum Chemical Probes of Electron-Transfer Kinetics: the Nature of Donor–Acceptor Interactions. *Chem. Rev.* **1991**, *91*, 767–792.
- (62) Lunt, R. R.; Benziger, J. B.; Forrest, S. R. Relationship between Crystalline Order and Exciton Diffusion Length in Molecular Organic Semiconductors. *Adv. Mater.* **2010**, *22*, 1233–1236.
- (63) Ros, M. B.; Serrano, J. L.; de la Fuente, M. R.; Folcia, C. L. Banana-Shaped Liquid Crystals: A New Field to Explore. *J. Mater. Chem.* **2005**, *15*, 5093–5098.
- (64) Henson, Z. B.; Welch, G. C.; van der Poll, T.; Bazan, G. C. Pyridalthiadiazole-Based Narrow Band Gap Chromophores. *J. Am. Chem. Soc.* **2012**, *134*, 3766–3779.
- (65) Kraabel, B.; Moses, D.; Heeger, A. J. Direct Observation of the Intersystem Crossing in Poly(3-octylthiophene). *J. Chem. Phys.* **1995**, *103*, 5102–5108.
- (66) Tsoi, W. C.; Spencer, S. J.; Yang, L.; Ballantyne, A. M.; Nicholson, P. G.; Turnbull, A.; Shard, A. G.; Murphy, C. E.; Bradley, D. D. C.; Nelson, J.; et al. Effect of Crystallization on the Electronic Energy Levels and Thin Film Morphology of P3HT:PCBM Blends. *Macromolecules* **2011**, *44*, 2944–2952.
- (67) Martin, R. L. Natural Transition Orbitals. *J. Chem. Phys.* **2003**, *118*, 4775–4777.
- (68) Franco, I.; Tretiak, S. Electron-Vibrational Dynamics of Photoexcited Polyfluorenes. *J. Am. Chem. Soc.* **2004**, *126*, 12130–12140.
- (69) Bixon, M.; Jortner, J., Eds.; *Advances in Chemical Physics*; John Wiley & Sons, Inc.: New York, 2007; pp 35–202.
- (70) Spano, F. C. The Spectral Signatures of Frenkel Polarons in H- and J-Aggregates. *Acc. Chem. Res.* **2010**, *43*, 429–439.
- (71) Beljonne, D.; Curutchet, C.; Scholes, G. D.; Silbey, R. J. Beyond Förster Resonance Energy Transfer in Biological and Nanoscale Systems. *J. Phys. Chem. B* **2009**, *113*, 6583–6599.
- (72) Nelson, T.; Fernandez-Alberti, S.; Chernyak, V.; Roitberg, A. E.; Tretiak, S. Nonadiabatic Excited-State Molecular Dynamics Modeling of Photoinduced Dynamics in Conjugated Molecules. *J. Phys. Chem. B* **2011**, *115*, 5402–5414.
- (73) Clark, J.; Nelson, T.; Tretiak, S.; Cirmi, G.; Lanzani, G. Femtosecond Torsional Relaxation. *Nat. Phys.* **2012**, *8*, 225–231.
- (74) Martinelli, N. G.; Olivier, Y.; Athanasopoulos, S.; Ruiz Delgado, M.-C.; Pigg, K. R.; da Silva Filho, D. A.; Sánchez-Carrera, R. S.; Venuti, E.; Della Valle, R. G.; Brédas, J.-L.; et al. Influence of Intermolecular Vibrations on the Electronic Coupling in Organic Semiconductors: The Case of Anthracene and Perfluoropentacene. *ChemPhysChem* **2009**, *10*, 2265–2273.
- (75) Sun, M.; Kjellberg, P.; Beenken, W. J. D.; Pullerits, T. Comparison of the Electronic Structure of PPV and Its Derivative DIOXA-PPV. *Chem. Phys.* **2006**, *327*, 474–484.
- (76) Cardona, C. M.; Li, W.; Kaifer, A. E.; Stockdale, D.; Bazan, G. C. Electrochemical Considerations for Determining Absolute Frontier

Orbital Energy Levels of Conjugated Polymers for Solar Cell Applications. *Adv. Mater.* **2011**, *23*, 2367–2371.

(77) Djurovich, P. I.; Mayo, E. I.; Forrest, S. R.; Thompson, M. E. Measurement of the Lowest Unoccupied Molecular Orbital Energies of Molecular Organic Semiconductors. *Org. Electron.* **2009**, *10*, 515–520.

(78) Kaake, L. G.; Welch, G. C.; Moses, D.; Bazan, G. C.; Heeger, A. J. Influence of Processing Additives on Charge-Transfer Time Scales and Sound Velocity in Organic Bulk Heterojunction Films. *J. Phys. Chem. Lett.* **2012**, *3*, 1253–1257.

(79) Yang, P.; Batista, E. R.; Tretiak, S.; Saxena, A.; Martin, R. L.; Smith, D. L. Effect of Intramolecular Disorder and Intermolecular Electronic Interactions on the Electronic Structure of Poly-*p*-phenylene Vinylene. *Phys. Rev. B* **2007**, *76*, 241201.

Supporting Information for

Ab-initio Study of a Molecular Crystal for Photovoltaics: Light Absorption, Exciton and Charge Carrier Transport

Andriy Zhugayevych,[†] Olena Postupna,^{†,‡} Ronald C. Bakus II, Gregory C. Welch,[§] Guillermo C. Bazan^{*§}
Sergei Tretiak^{*†}

[†] Theoretical Division, Center for Nonlinear Studies and Center for Integrated Nanotechnologies, Los Alamos National Laboratory, Los Alamos, NM 87545, USA

[‡] Department of Chemistry, University of Rochester, Rochester, NY 14627, USA

[§] Departments of Materials and Chemistry & Biochemistry, Center for Polymers and Organic Solids, University of California, Santa Barbara, California 93106, USA

Molecular orbitals

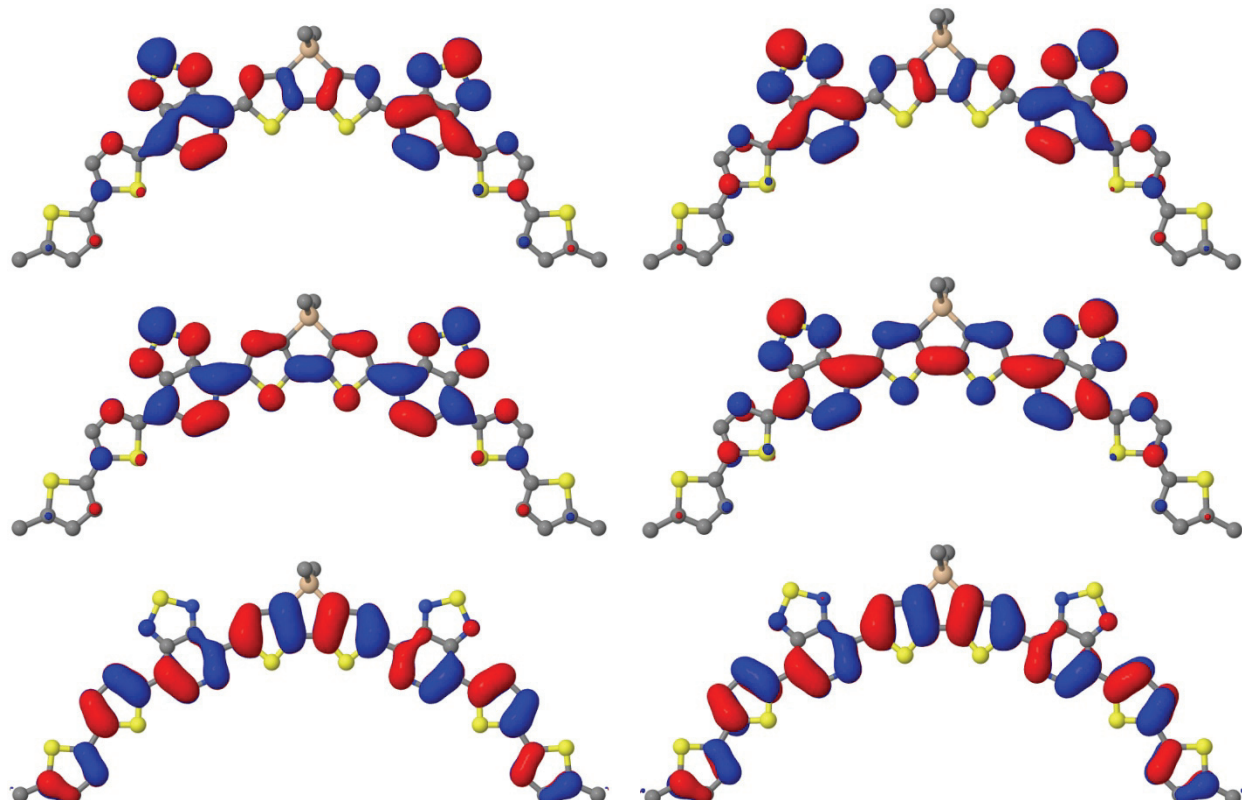


Figure S1. Two LUMOs and HOMO (from top to bottom) for a molecule in the experimentally determined geometry in crystal (left) and in the optimized geometry in chloroform solution (right). Hydrogens and aliphatic chains are not shown.

Displaced harmonic oscillator model

Here we state and explain some facts of the independent boson¹ or displaced harmonic oscillator model² used in the analysis of experimental spectra. The transition spectral density $\rho(E)$ of this model can be conveniently represented as the Fourier transform

$$\rho(E) = \frac{1}{2\pi\hbar} \int_{-\infty}^{\infty} \hat{\rho}(t) e^{itE/\hbar} dt \quad (\text{S1})$$

of the phonon time correlation function

$$\hat{\rho}(t) = \exp \left[\sum_{\alpha} S_{\alpha} \left(\coth \frac{\hbar\omega_{\alpha}}{2kT} (\cos \omega_{\alpha} t - 1) - i \sin \omega_{\alpha} t \right) - i \frac{E_{00}}{\hbar} t \right] \hat{\delta}(t), \quad (\text{S2})$$

where ω_{α} and S_{α} are vibrational frequencies and the corresponding Huang–Rhys factors, the sum is over all the vibratioanl modes, E_{00} is the 0-0 transition energy, T is the temperature, and $\hat{\delta}$ is the lineshape function. For the latter we take the unbiased Gaussian function $\hat{\delta}(t) = \exp(-\sigma^2 t^2 / 2\hbar^2)$ to describe an inhomogeneous broadening or fluctuations of single-molecule properties.

If the line broadening is large enough (usually the spectrum will look structureless), either due to large σ or due to large number of low-frequency modes of the molecule itself (our case), the $\ln \hat{\rho}(t)$ is nearly quadratic in the large region of the complex plane around the saddle-point $t = -\frac{i\hbar}{2kT}$ of the sum in (S2):

$$\hat{\rho}(t) \approx \exp \left[-S'' - i \frac{E_{00} + \lambda'}{\hbar} t - \frac{\sigma^2 + 2\lambda' T}{2\hbar^2} t^2 \right], \quad (\text{S3})$$

where the parameters λ' and S'' correspond to the exciton relaxation energy due to the “classical” modes and total Huang–Rhys factor of the “quantum” modes, respectively. For $E = E_{00} - \frac{\sigma^2}{2kT}$ the above point is also the saddle-point of the integrand in (S1) and we obtain Formula (3) of the main text. More accurate approximation replaces S'' in (S3) by the effective quantum mode:

$$\hat{\rho}(t) \approx \exp \left[C + S'' \left(\coth \frac{\hbar\omega''}{2kT} (\cos \omega'' t - 1) - i \sin \omega'' t \right) - i \frac{E_{00} + \lambda'}{\hbar} t - \frac{\sigma^2 + 2\lambda' T}{2\hbar^2} t^2 \right], \quad (\text{S4})$$

where C is nearly zero. We will use this approximation with the parameters $\lambda', S'', \hbar\omega'', C$ determined by matching the function and its derivatives at the saddle-point.

The mean energy and dispersion of the transition spectral density are given by

$$\bar{E} = E_{00} + \lambda, \quad \mathbb{D}E = \sum_{\alpha} S_{\alpha} \hbar^2 \omega_{\alpha}^2 \coth \frac{\hbar\omega_{\alpha}}{2kT} + \sigma^2, \quad (\text{S5})$$

where

$$\lambda = \sum_{\alpha} S_{\alpha} \hbar \omega_{\alpha} \quad (\text{S6})$$

is the exciton (or polaron) relaxation energy. From known λ , $\mathbb{D}E$, λ' , S'' , and σ we can obtain $\hbar\omega''$ entering (S4) by the two alternative formulas:

$$\hbar\omega'' = \frac{\lambda - \lambda'}{S''}, \quad (\text{S7})$$

$$\hbar\omega'' = \sqrt{\frac{\mathbb{D}E - 2\lambda' kT - \sigma^2}{S''}}, \quad (\text{S8})$$

that can be used to cross-check the analysis of experimental spectra.

¹Mahan G D, Many-particle physics (Plenum, 1990).

²P O J Scherer, S F Fischer, Theoretical Molecular Biophysics (Springer, 2010).

Ab-initio calculations used in the analysis of experimental spectra

	$E_2 - E_1$ (eV)	OS_2/OS_1
B3LYP	0.37	0.10
CAM-B3LYP (6-31g)	0.36	0.21
CAM-B3LYP (in vacuo)	0.39	0.23
CAM-B3LYP	0.39	0.23
M06-2X	0.39	0.24
wB97X	0.40	0.24

Table S1. Energy and oscillator strength of the second transition relative to the first one calculated by different methods. By default the basis set is 6-31g* and the CPCM medium is chloroform.

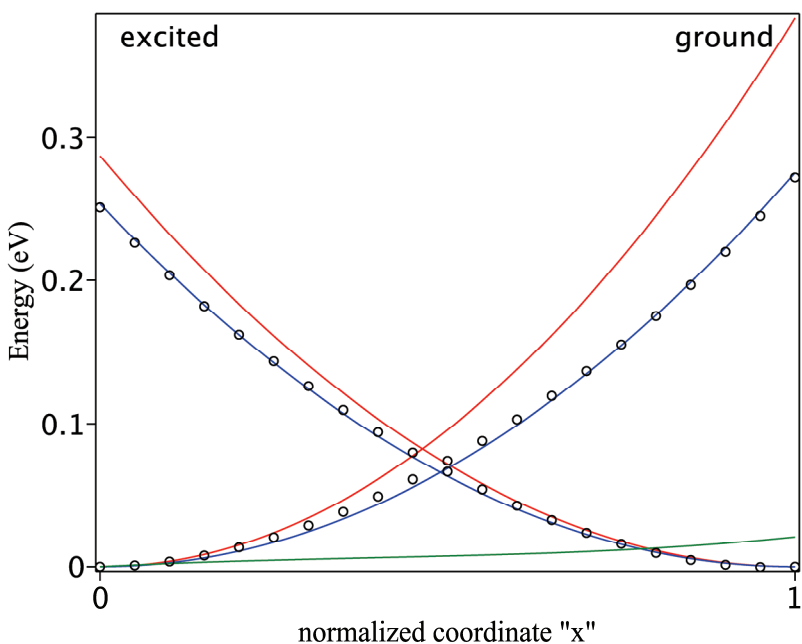


Figure S2. Linear potential energy scans (dots) along the reaction coordinate for the first excitation transition for the molecule in both ground and excited states. Blue lines are harmonic fits to these curves, green line is their difference. Red lines correspond to the harmonic potential surfaces with the vibrational modes calculated in the potential minimums.

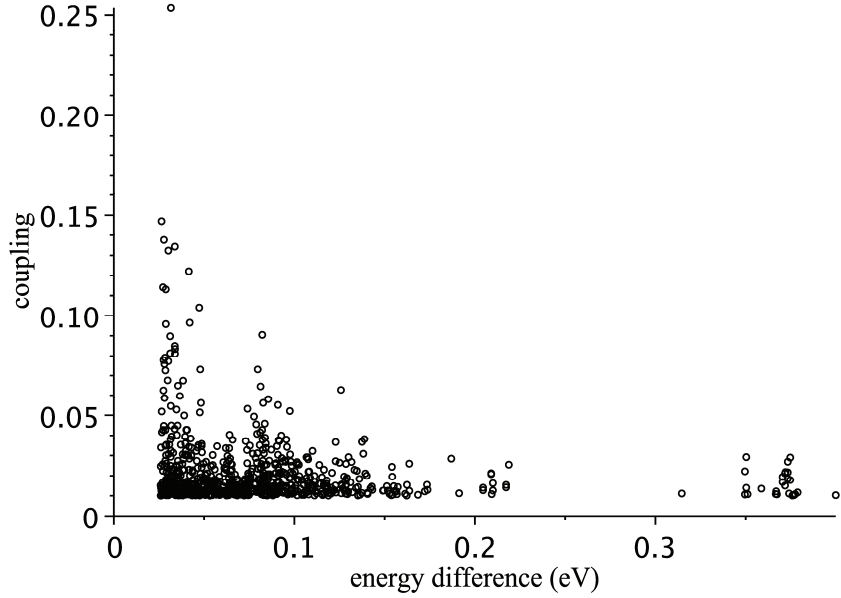


Figure S3. Analysis of the Duschinsky matrix (J): for each pair of vibrational modes $|J_{ij}|$ is plotted against the energy difference $|E_i - E_j|$ of these modes. Points for which $|E_i - E_j| < kT$, or $|J_{ij}| < 0.01$, or both Huang-Rhys factors are smaller than 0.02 are not shown.

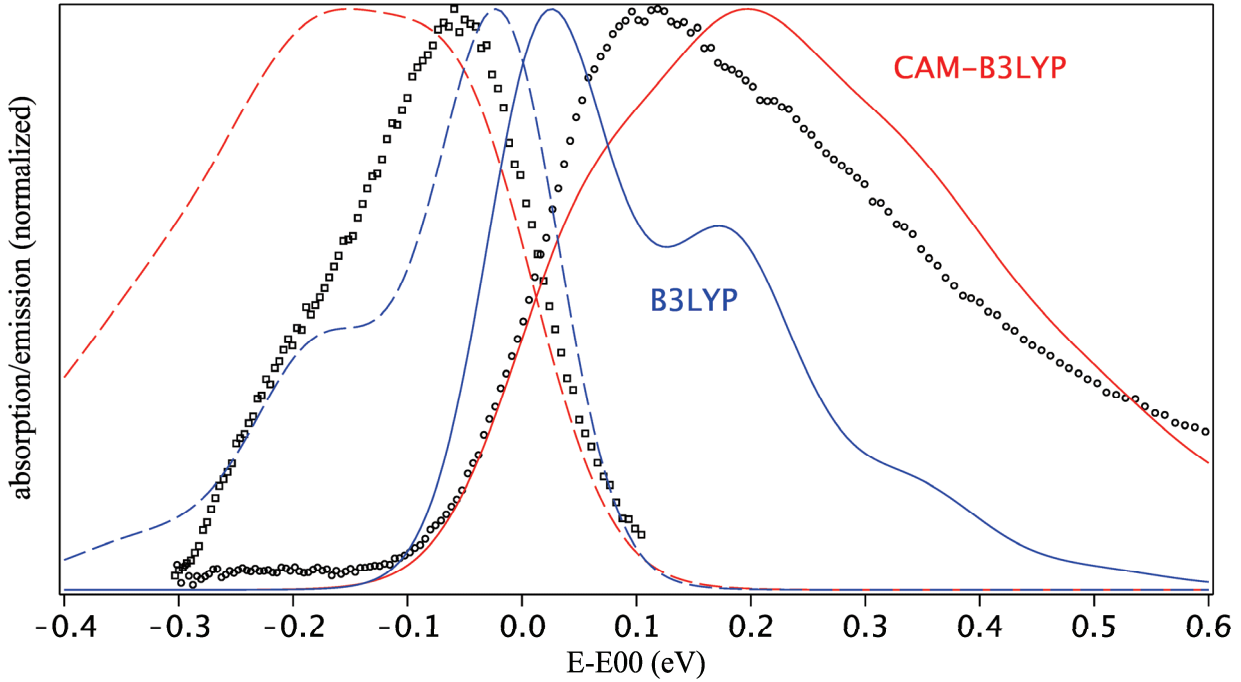


Figure S4. Calculated emission (dash lines) and absorption (solid lines) spectra compared to the experimental fluorescence emission (squares) and excitation (circles) spectra. Because the Duschinsky matrix is nearly diagonal, see Figure S3, the displaced harmonic oscillator model is used. In CAM-B3LYP calculations all the frequencies and Huang-Rhys factors are rescaled by the same number to match the exact potential energy profile in Figure S2 (in this match we fix the transformation matrix between Cartesian and normal coordinates).

Analysis of experimental spectra

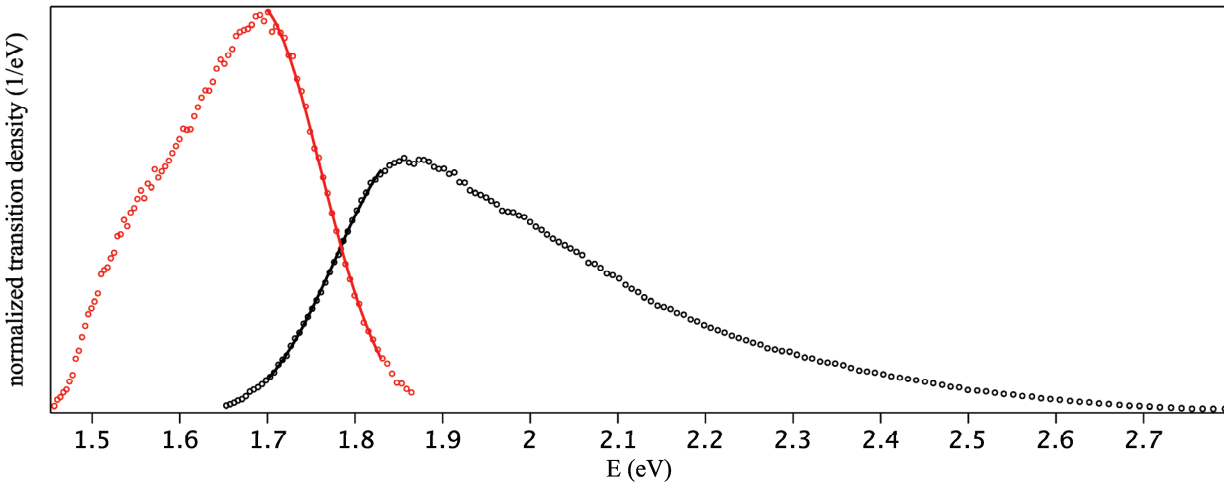


Figure S5. Experimental transition spectral densities for the emission (red, fluorescence emission) and absorption (black, fluorescence excitation), and the Gaussian fits to the spectral edges. The spectral overlap is the integral of the product of the shown functions. The experimental absorption spectrum is cut at 2.8 eV to leave only the first two electronic transitions. Because the second transition, shifted by 0.4 eV with respect to the first, cannot be isolated the transition density for the absorption is normalized to 1.23 to take into account the contribution of the second transition (see Table S1).

polynomial coefficients	emission			absorption		
	C ₀	C ₁	C ₂	C ₀	C ₁	C ₂
estimate	-262.0	312.3	-92.6	-238.0	256.5	-68.8
standard deviation	9.5	10.7	3.0	7.0	7.9	2.2

Table S2. Details on the least squares quadratic fit to the natural logarithm of the emission and absorption transition spectral densities. The fitting range is 1.70-1.83 eV.

	experiment		CAM-B3LYP		B3LYP	
	by (S7)	by (S8)	by fit	by (S4)	by fit	by (S4)
λ_{abs} (eV)	0.20		0.27		0.12	
λ'_{abs} (eV)	0.11		0.08	0.07	0.03	0.03
S''_{abs}	0.45		1.05	1.22	0.56	0.56
$\hbar\omega''_{\text{abs}}$ (eV)	0.21	0.22	0.10	0.15	0.06	0.16
λ_{emi} (eV)	0.10		0.25		0.11	
λ'_{emi} (eV)	0.07		—		—	
S''_{emi}	0.18		—		—	
$\hbar\omega''_{\text{emi}}$ (eV)	0.14	0.11	—		—	
σ (eV)	0.04		—		—	
E_{00} (eV)	1.76		1.96		1.35	
J (eV ⁻¹)	0.57		0.15		1.35	

Table S3. Summary of the analysis of experimental spectra and the comparison with ab-initio calculations. Cross-check analysis given in columns "by (S7)" and "by (S8)" is based on the fact that the parameters determined from the 0-0 edge fit and mean energy and bandwidth of the emission and absorption transition spectral densities are not independent. When calculating the mean energy and bandwidth for the absorption, we use the following parameters for the second transition relative to the first transition (see Table S1): peak position shift 0.4 eV, oscillator strengths ratio 0.23, dispersions ratio 1 (it is a guess). The column "by fit" uses Formula (3) of the main text with the fitting range chosen to cover 90% of the spectral overlap.

Exciton intermolecular couplings

Transfer integrals (intermolecular couplings) entering the Holstein Hamiltonian for excitons can be estimated from the dimer calculations in the following way. In this approximation we estimate the parameters of the effective Hamiltonian

$$H = \begin{pmatrix} \varepsilon_1 & t \\ t & \varepsilon_2 \end{pmatrix} \quad (\text{S9})$$

using the results of high-level calculations; here t is the transfer integral and $\varepsilon_{1,2}$ are the on-site energies, the basis set is assumed to be orthogonal. The eigenvalues and eigenvectors of this Hamiltonian should match the energies and wave-functions of the two lowest electronic states of the dimer. While the energies can be directly taken from the output of the high-level calculations, the treatment of the wave-functions is cumbersome. The alternative way we chose is to use electric transition dipoles to estimate the eigenvectors of H . The algorithm is as follows.

First, we need six quantities be obtained in high-level calculations: electric transition dipoles, \mathbf{d}_1 , \mathbf{d}_2 , for the studied transition for both monomers, the corresponding excitation energies, E_1 , E_2 , and dipoles, \mathbf{D}_1 , \mathbf{D}_2 , for the dimer. Then, we match thus obtained $\mathbf{D}_{1,2}$ with the prediction of the dimer approximation:

$$(\mathbf{D}_1^{\text{approx}} \quad \mathbf{D}_2^{\text{approx}}) = (\mathbf{d}_1 \quad \mathbf{d}_2) T, \quad (\text{S10})$$

where T is 2×2 matrix whose columns are eigenvectors of H . The matrix T is determined by minimizing the deviation

$$\Delta = (\mathbf{D}_1^{\text{approx}} - \mathbf{D}_1)^2 + (\mathbf{D}_2^{\text{approx}} - \mathbf{D}_2)^2. \quad (\text{S11})$$

To give an explicit solution, we note that T can be either:

$$T' = \begin{pmatrix} \cos \alpha' & -\sin \alpha' \\ \sin \alpha' & \cos \alpha' \end{pmatrix} \text{ or } T'' = \begin{pmatrix} \sin \alpha'' & \cos \alpha'' \\ \cos \alpha'' & -\sin \alpha'' \end{pmatrix}. \quad (\text{S12})$$

By substituting T' into (S10) and minimizing (S11) we obtain

$$\alpha' = \text{atan2}(\mathbf{D}_1 \mathbf{d}_2 - \mathbf{D}_2 \mathbf{d}_1, \mathbf{D}_1 \mathbf{d}_1 + \mathbf{D}_2 \mathbf{d}_2), \quad (\text{S13})$$

$$\Delta' = D_1^2 + D_2^2 + d_1^2 + d_2^2 - 2\sqrt{(\mathbf{D}_1 \mathbf{d}_2 - \mathbf{D}_2 \mathbf{d}_1)^2 + (\mathbf{D}_1 \mathbf{d}_1 + \mathbf{D}_2 \mathbf{d}_2)^2}, \quad (\text{S14})$$

and then

$$\varepsilon_1 = E_1 \cos^2 \alpha' + E_2 \sin^2 \alpha', \quad \varepsilon_2 = E_1 \sin^2 \alpha' + E_2 \cos^2 \alpha', \quad t = (E_1 - E_2) \sin \alpha' \cos \alpha'. \quad (\text{S15})$$

The second solution, α'' , can be obtained by exchanging indexes 1,2 at \mathbf{d} and ε in the above formulas. Among these two solutions we chose the one with smaller Δ .

Because the sign of a transition dipole is not defined, we cannot decide between which ε is 1 and which is 2. This means that the sign of $\varepsilon_1 - \varepsilon_2$ cannot be determined by the proposed method. Nevertheless the quantities $|\varepsilon_1 - \varepsilon_2|$, $\varepsilon_1 + \varepsilon_2$, and t are determined unambiguously.

For the studied dimers the approximation error, $\sqrt{\Delta/(d_1^2 + d_2^2)}$, rarely exceeds few percents.

The advantage of the above method as compared to the commonly used “half energy split” formula $t = |E' - E''|/2$ is twofold. First, the sign of t can be determined (generally we can neglect the sign only for one-dimensional aggregates). Second, the “half energy split” formula is valid only in the case of two identical monomers symmetrically composing the dimer (if the identical monomers are not symmetry-equivalent in the dimer then the Davydov splitting must be taken into account).

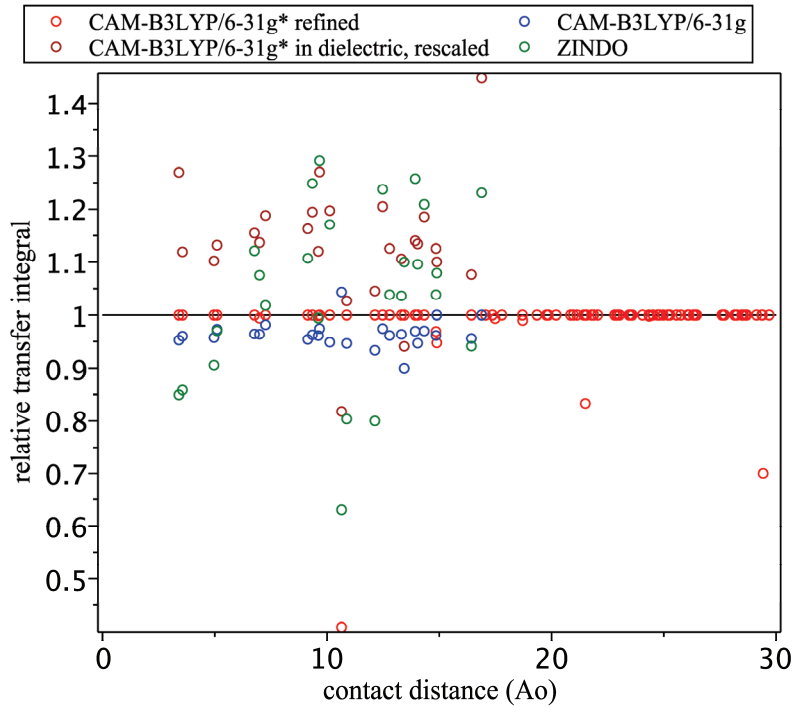


Figure S6. Various methods for calculating exciton couplings (transfer integrals) in the dimer approximation are compared to half energy split approach by CAM-B3LYP/6-31g* in vacuo. Here “refined” (red dots) means more accurate calculations described below. Transfer integrals calculated within CPCM in chloroform (brown dots) are multiplied by the optical dielectric constant of the medium.

state	E-E _{monomer} (meV)		transition dipole (eÅ)	
	Ab-initio	TB	Ab-initio	TB
1	-75	-77	0	0
2	-52	-54	(-0.37, 0.07, -0.80)	(-0.49, 0, -0.95)
3	+8	+16	0	0
4	+112	+132	(2.09, -0.24, 4.78)	(2.70, 0, 5.27)

Table S4. Comparison of excited state energies and transition dipoles for a stack of four molecules calculated by ab-initio method (CAM-B3LYP/6-31g*) and by tight-binding (TB) approach with the parameters determined in the dimer approximation using the same ab-initio method.

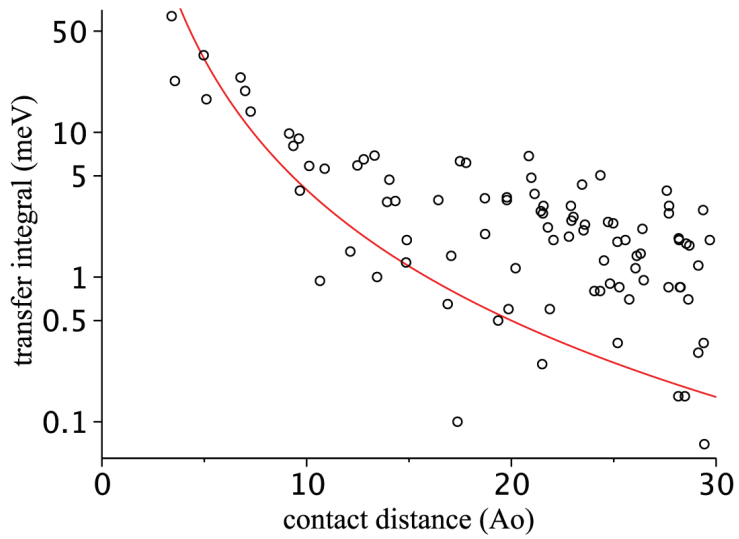


Figure S7. Dependence of exciton intermolecular couplings (transfer integrals) on contact distance between the molecules. All couplings within contact distance of 30 Å are shown. Red line shows r^3 dependence expected for dipole-dipole interaction.

Analysis of exciton transport regime

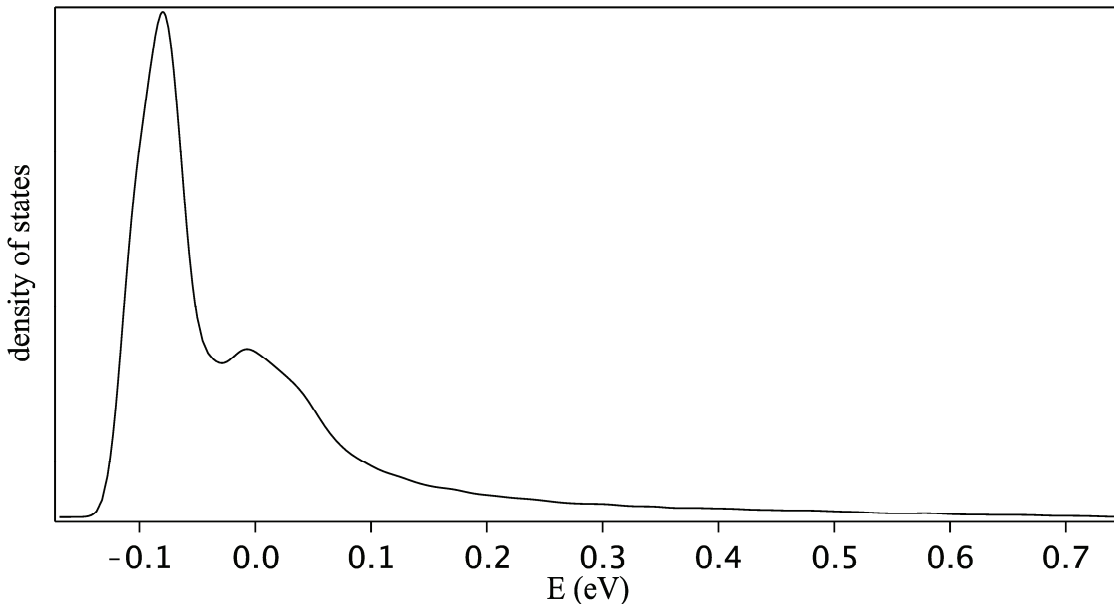


Figure S8. Density of states for un-relaxed excitons. The energy is counted with respect to the single molecule exciton.

Let's now discuss other possible regimes of exciton transport. First of all, the exciton binding energy calculated as

$$E_{\text{cation}} + E_{\text{anion}} - E_{\text{exciton}} - E_{\text{ground}}$$

is about 0.4-0.6 eV with or without the relaxation effects (the calculations are performed in the solution to mimic the effects of crystalline environment). This value far exceeds the intermolecular couplings, therefore the assumption of Frenkel type of exciton is correct.

To answer the questions of whether the relaxed exciton is stable and whether it is localized (no polaron bands) we need to consider delocalized excitons. Complete treatment of excitons and vibrations in extended systems is possible only for much simpler cases, that is why we consider the tight-binding Hamiltonian for excitons and neglect vibronic couplings in zero order approximation. Because all molecules in the considered crystal are equivalent by symmetry the diagonal elements of the Hamiltonian are zero; the non-diagonal elements are exciton couplings (the sign of each coupling is determined by comparing the transition dipoles for dimer and its monomers). In our calculations we neglect couplings for the contact intermolecular separations larger than 30 Å. The resulting error in band energies at small wave-vectors is of the order of squared dipole moment divided by the distance between the nearest neighbor molecules, which is 0.1 eV. Nevertheless for quantities integrated over the wave-vectors the error will be much smaller.

The calculated density of states is shown in Figure S8. The effective bandwidth is about 0.2 eV, since 85% of the states are concentrated in the region between -0.1 and 0.1 eV. The bandwidth is much larger than the room temperature, therefore a thermal disorder cannot localize excitons. On the other side, the gain in energy due to the delocalization is about 0.1 eV which is

slightly smaller than the gain due to the intramolecular geometry relaxation given by $\lambda/2=0.2$ eV. Therefore excitons seem to be localized by strong vibronic couplings.

To check if relaxed excitons are delocalized (polaron bands) we need to estimate the phonon-renormalized exciton couplings. They can be written as

$$t' = t e^{-A_{\text{abs}} - A_{\text{emi}}}$$

where for each, absorption and emission,

$$A = \frac{1}{2} \sum_i S_i \coth \frac{\hbar \omega_i}{2kT}$$

and the sum is over all the vibrational modes. To estimate A from the experimentally determined effective λ for classic modes and effective S for quantum modes (see the previous section) we split the above sum into low- and high-frequency modes at some ω_0 of the order of kT/\hbar . Then we replace the low-frequency sum by continuous distribution of modes with the spectral density $\rho(\omega)$, approximate $\rho(\omega)S(\omega)$ by a power-law dependence ω^α , using the identity

$$\lambda = \int_0^{\omega_0} \rho(\omega)S(\omega) \hbar \omega d\omega$$

to determine the normalization constant. In the high-frequency sum we replace the coth-function by unity. The result is

$$A_{\text{abs}} + A_{\text{emi}} = c \frac{\lambda_{\text{abs}} + \lambda_{\text{emi}}}{kT} + \frac{S_{\text{abs}} + S_{\text{emi}}}{2}$$

where c depends on ω_0 and α . To make the lower estimate for c we take $\alpha=2$ (no higher than three dimensional density of states, uniform distribution of Huang-Rhys factors) and $\omega_0=2kT/\hbar$ (this will be definitely a quantum mode). For this values of the parameters $c=0.4$ and the resulting estimate is $t'/t < 0.04$, putting both the couplings and the bandwidth (-0.1 to 0.1 eV non-renormalized, see Figure S8) well below kT for room temperatures. Therefore the relaxed excitons move by hopping.

Ab-initio estimates (CAM-B3LYP, B3LYP) give negligible t' .

Formulas for diffusion tensor and length

Let X be a translationally invariant d -dimensional lattice so that each point $x \in X$ can be presented as $x = (\xi, \alpha)$, where ξ runs \mathbb{Z}^d and α runs the unit cell. Let \mathbf{T} be the set of the translation vectors and \mathbf{r}^α is the vector of Euclidean coordinates of the site α in the unit cell. We will use indexes $i, j = \overline{1, d}$ to enumerate Euclidean coordinates and the lattice dimensions.

Consider the kinetic equation on X :

$$\dot{p}_x = -p_x(\nu_x + w_x) + \sum_z p_z w_{zx},$$

where w_{zx} is the transition rate from z to x and $w_x = \sum_z w_{xz}$, here and throughout the text a sum without limits means the sum over all possible values of the indicated variable. The Green's function of the kinetic equation, $G_{yx}(s)$, which is the Laplace transform of the transition probability $p_{yx}(t)$, satisfies the equation

$$(s + \nu_x + w_x)G_{yx} - \delta_{yx} = \sum_z G_{yz} w_{zx}.$$

Because of the translational invariance

$$\nu_{(\xi, \alpha)} = \nu^\alpha, \quad w_{(\xi, \alpha)} = w^\alpha, \quad w_{(\eta, \beta)(\xi, \alpha)} = w_{\xi-\eta}^{\beta\alpha}, \quad G_{(\eta, \beta)(\xi, \alpha)} = G_{\xi-\eta}^{\beta\alpha}.$$

Denote

$$\hat{G}^{\beta\alpha} = \sum_\xi G_\xi^{\beta\alpha}.$$

It satisfies the equation

$$(s + \nu^\alpha + w^\alpha)\hat{G}^{\beta\alpha} - \delta^{\beta\alpha} = \sum_{\gamma\xi} \hat{G}^{\beta\gamma} w_\xi^{\gamma\alpha}.$$

At small s

$$\hat{G}^{\beta\alpha}(s) = s^{-1} p^{\beta\alpha}(\infty) + R^{\beta\alpha} + o(1).$$

In the introduced notations the diffusion tensor can be calculated by the following formula:

$$\mathbf{D} = \frac{1}{2} \sum_{ij} \sum_\gamma p^{\beta\gamma}(\infty) \left(\sum_{\delta\xi} w_\xi^{\gamma\delta} \xi_i \xi_j + \sum_{\delta\lambda\mu\xi\eta} w_\xi^{\gamma\delta} R^{\delta\lambda} w_\eta^{\lambda\mu} (\xi_i \eta_j + \eta_i \xi_j) \right) \mathbf{T}_i \otimes \mathbf{T}_j.$$

Note that in the ergodic case \mathbf{D} does not depend on β . If $\nu > 0$ then $p^{\beta\alpha}(\infty) = 0$. In this case the tensor Λ can be calculated by the following formula:

$$\begin{aligned} \mathbf{\Lambda} = \frac{1}{2} \sum_{ij} \left[\sum_\gamma R^{\beta\gamma} \left(\sum_{\delta\xi} w_\xi^{\gamma\delta} \xi_i \xi_j + \sum_{\delta\lambda\mu\xi\eta} w_\xi^{\gamma\delta} R^{\delta\lambda} w_\eta^{\lambda\mu} (\xi_i \eta_j + \eta_i \xi_j) \right) \mathbf{T}_i \otimes \mathbf{T}_j \right. \\ \left. + \sum_{\gamma\delta\xi} R^{\beta\gamma} w_\xi^{\gamma\delta} R^{\delta\alpha} \nu^\alpha (\xi_i \mathbf{T}_i \otimes \mathbf{r}_j^\alpha + \xi_j \mathbf{r}_i^\alpha \otimes \mathbf{T}_j) + \sum_\alpha R^{\beta\alpha} \nu^\alpha (\mathbf{r}_i^\alpha \otimes \mathbf{r}_j^\alpha) \right]. \end{aligned}$$

Synthesis and structural characterization

DTS(PTTh₂)₂ was prepared according to the literature procedure.¹ Single crystals of DTS(PTTh₂)₂ were grown by slow vapor diffusion of acetone into a dichloromethane solution at 4°C. Data collection was performed on a Bruker Kappa Apex II ($\lambda = 0.71073\text{\AA}$, 50kV/ 30mA) at 100K, with a fine focus sealed tube as the X-ray source. ω -scans collected with Bruker AXS APEX2 software² yielded 6150 unique reflections. The intensities were integrated and the Lorenz and polarization corrections applied using SAINT.² Absorption and volume corrections were made using SADABS.³ The structure was solved in SHELXS-97 using direct methods, and refined in SHELXL-97 using full-matrix least-squares on F².⁴ In the hexyl and π -conjugated portions of the molecule, all non-hydrogen atoms were refined with anisotropic displacement parameters, and hydrogens were placed in idealized positions and refined using isotropic displacement factors. Because the 2-ethylhexyl chains exist as superimposed R/S isomers, the anisotropic displacement parameters for the carbons could not be determined from the x-ray data. Therefore, the chains were modeled using constrained geometric parameters and isotropic temperature factors as follows: the R and S fragments were modeled by constraining the C-C and C-Si bond lengths and temperature factors to be the same for each fragment, with optimized occupancy being near equal. The hydrogens in the 2-ethylhexyl chain were not modeled.

DTS(PTTh₂)₂ crystal data: Monoclinic $C2/c$, $a = 39.3141(14)\text{\AA}$, $b = 15.2065(5)\text{\AA}$, $c = 10.3691(3)\text{\AA}$, $\beta = 103.575(2)^\circ$, $V = 6025.8(3)\text{\AA}^3$, $Z = 4$, $R = 0.0711$.

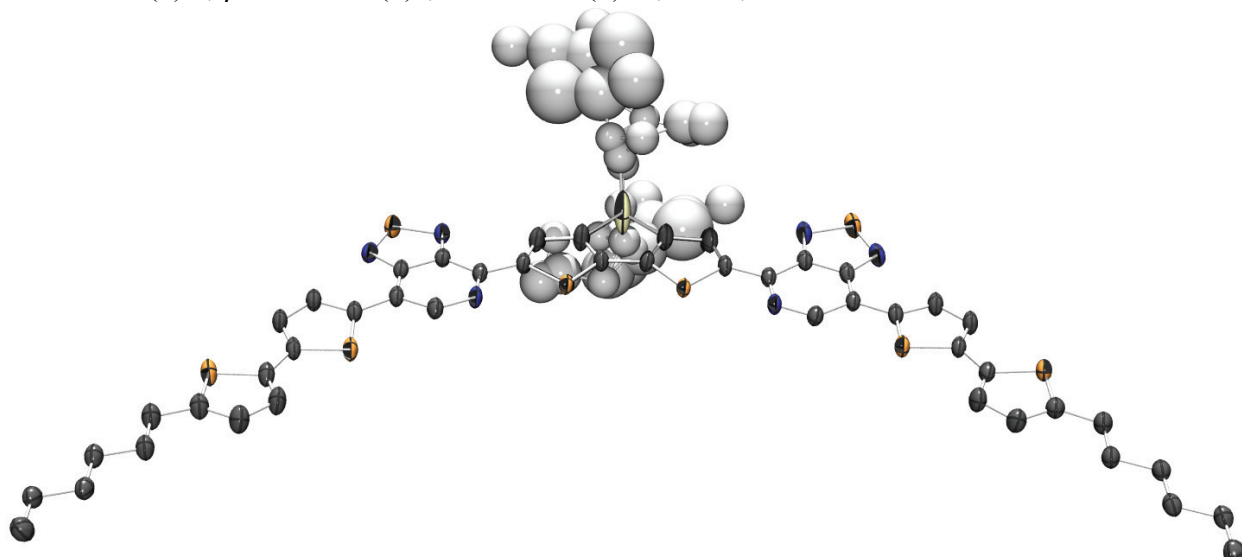


Figure S9. Solid state structure of DTS(PTTh₂)₂ (carbons in dark grey, silicon in yellow, sulfur in orange, nitrogen in blue, disordered carbons pictured in lighter grey, and hydrogens excluded for clarity).

¹ Sun, Y.; Welch, G. C.; Leong, W. L.; Takacs, C. J.; Bazan, G. C.; Heeger A. J. *Nature Materials*, **2012**, *11*, 44-48.

² APEX2 and SAINT Software Bruker AXS, Inc., Madison, WI, 2011.

³ G. M. Sheldrick, SADABS, Software for Empirical Absorption Correction, Bruker AXS, Inc., Madison, WI, 2008.

⁴ SHELXTL Sheldrick, G. M. *Acta Crystallogr., Sect. A*, **2008**, *64*, 112.

Table S5. Crystal data and structure refinement for DTS(PTTh₂)₂.

Identification code	DTS(PTTh ₂) ₂		
Empirical formula	C ₆₂ H ₇₂ N ₆ S ₈ Si		
Formula weight	1185.83		
Temperature	100(2) K		
Wavelength	0.71073 Å		
Crystal system	Monoclinic		
Space group	C2/c		
Unit cell dimensions	a = 39.3141(14) Å	α = 90°.	
	b = 15.2065(5) Å	β = 103.575(2)°.	
	c = 10.3691(3) Å	γ = 90°.	
Volume	6025.8(3) Å ³		
Z	4		
Density (calculated)	1.307 Mg/m ³		
Absorption coefficient	0.361 mm ⁻¹		
F(000)	2512		
Crystal size	0.30 x 0.20 x 0.20 mm ³		
Theta range for data collection	2.09 to 26.37°		
Index ranges	-49<=h<=49, -16<=k<=18, -12<=l<=12		
Reflections collected	15430		
Independent reflections	6150 [R(int) = 0.0299]		
Completeness to theta = 26.37°	99.9 %		
Absorption correction	Semi-empirical from equivalents		
Max. and min. transmission	0.7454 and 0.6484		
Refinement method	Full-matrix least-squares on F ²		
Data / restraints / parameters	6150 / 30 / 334		
Goodness-of-fit on F ²	1.325		
Final R indices [I>2sigma(I)]	R1 = 0.0711, wR2 = 0.1716		
R indices (all data)	R1 = 0.0973, wR2 = 0.1847		
Largest diff. peak and hole	1.148 and -1.015 e.Å ⁻³		

Table S6. Atomic coordinates ($\text{\AA} \times 10^4$) and equivalent isotropic displacement parameters ($\text{\AA}^2 \times 10^3$). U(eq) is defined as one third of the trace of the orthogonalized U^{ij} tensor.

	x	y	z	U(eq)
C(1)	3069(1)	-2986(3)	17683(4)	57(1)
C(2)	3031(1)	-2003(3)	17600(4)	44(1)
C(3)	2768(1)	-1693(3)	16353(4)	45(1)
C(4)	2737(1)	-701(3)	16256(4)	44(1)
C(5)	2471(1)	-380(3)	15016(4)	47(1)
C(6)	2449(1)	615(3)	14991(4)	51(1)
C(7)	2193(1)	1006(3)	13817(4)	49(1)
C(8)	1984(1)	608(3)	12732(4)	56(1)
C(9)	1789(1)	1218(3)	11802(4)	56(1)
C(10)	1851(1)	2070(3)	12164(4)	45(1)
C(11)	1726(1)	2883(3)	11491(4)	44(1)
C(12)	1819(1)	3723(3)	11878(4)	47(1)
C(13)	1658(1)	4373(3)	10982(4)	47(1)
C(14)	1434(1)	4020(3)	9864(3)	42(1)
C(15)	1227(1)	4484(3)	8720(3)	40(1)
C(16)	1031(1)	4045(3)	7624(4)	41(1)
C(17)	1204(1)	5412(3)	8642(3)	40(1)
C(18)	981(1)	5824(3)	7511(3)	40(1)
C(19)	786(1)	5281(3)	6455(3)	39(1)
C(20)	550(1)	5642(3)	5276(3)	41(1)
C(21)	469(1)	6483(3)	4916(4)	53(1)
C(22)	225(1)	6576(3)	3684(4)	58(1)
C(23)	126(1)	5759(3)	3134(4)	41(1)
C(25A)	-349(3)	7912(11)	3172(14)	116(4)
C(26A)	-348(3)	8661(8)	4185(12)	102(3)
C(27A)	-57(4)	8446(11)	5399(14)	122(4)
C(28A)	-184(7)	7739(19)	6230(20)	201(7)
C(29A)	-694(4)	8672(13)	4580(20)	338(16)
C(30A)	-865(9)	9544(18)	4430(40)	450(20)
C(31A)	-869(13)	9973(17)	3100(20)	326(16)
C(32A)	-828(7)	10970(17)	3340(30)	185(7)
C(25B)	-166(3)	8407(6)	2899(14)	116(4)
C(26B)	-510(3)	8088(8)	3164(11)	102(3)
C(27B)	-471(4)	7496(8)	4302(14)	122(4)
C(28B)	-267(7)	7924(17)	5592(14)	201(7)
C(29B)	-735(5)	8888(13)	3300(20)	338(16)
C(30B)	-900(13)	9260(20)	1930(20)	450(20)
C(31B)	-1055(11)	10156(16)	2110(20)	326(16)
C(32B)	-1238(6)	10547(12)	810(20)	185(7)
N(1)	1371(1)	6003(3)	9542(3)	47(1)
N(2)	976(1)	6706(3)	7580(3)	47(1)
N(3)	818(1)	4421(3)	6537(3)	42(1)
S(1)	2149(1)	2128(1)	13698(1)	49(1)
S(2)	1425(1)	2880(1)	9972(1)	45(1)
S(3)	1242(1)	6964(1)	8972(1)	52(1)
S(4)	325(1)	4905(1)	4091(1)	36(1)
Si	0	7435(2)	2500	124(2)

Table S7. Bond lengths (\AA) and angles ($^\circ$) for DTS(PTTh₂)₂.

C(1)-C(2)	1.503(6)
C(1)-H(1A)	0.9800
C(1)-H(1B)	0.9800
C(1)-H(1C)	0.9800
C(2)-C(3)	1.527(5)
C(2)-H(2A)	0.9900
C(2)-H(2B)	0.9900
C(3)-C(4)	1.516(6)
C(3)-H(3A)	0.9900
C(3)-H(3B)	0.9900
C(4)-C(5)	1.533(5)
C(4)-H(4A)	0.9900
C(4)-H(4B)	0.9900
C(5)-C(6)	1.516(6)
C(5)-H(5A)	0.9900
C(5)-H(5B)	0.9900
C(6)-C(7)	1.507(5)
C(6)-H(6A)	0.9900
C(6)-H(6B)	0.9900
C(7)-C(8)	1.370(6)
C(7)-S(1)	1.716(5)
C(8)-C(9)	1.423(6)
C(8)-H(8)	0.9500
C(9)-C(10)	1.356(7)
C(9)-H(9)	0.9500
C(10)-C(11)	1.447(6)
C(10)-S(1)	1.742(4)
C(11)-C(12)	1.363(6)
C(11)-S(2)	1.734(4)
C(12)-C(13)	1.402(6)
C(12)-H(12)	0.9500
C(13)-C(14)	1.388(5)
C(13)-H(13)	0.9500
C(14)-C(15)	1.455(5)
C(14)-S(2)	1.737(5)
C(15)-C(16)	1.385(5)
C(15)-C(17)	1.415(6)
C(16)-N(3)	1.361(5)
C(16)-H(16)	0.9500
C(17)-N(1)	1.350(5)
C(17)-C(18)	1.433(5)
C(18)-N(2)	1.343(6)
C(18)-C(19)	1.440(5)
C(19)-N(3)	1.315(6)
C(19)-C(20)	1.457(5)
C(20)-C(21)	1.349(6)
C(20)-S(4)	1.743(4)
C(21)-C(22)	1.414(6)
C(21)-H(21)	0.9500
C(22)-C(23)	1.384(6)
C(22)-Si	1.867(5)
C(23)-C(23) ^{#1}	1.448(7)

C(23)-S(4)	1.709(4)
C(25A)-C(26A)	1.549(9)
C(25A)-Si	1.829(9)
C(26A)-C(29A)	1.508(9)
C(26A)-C(27A)	1.526(9)
C(27A)-C(28A)	1.531(10)
C(29A)-C(30A)	1.477(10)
C(30A)-C(31A)	1.528(10)
C(31A)-C(32A)	1.539(10)
C(25B)-C(26B)	1.523(9)
C(25B)-C(25B)#1	1.70(2)
C(25B)-Si	1.704(9)
C(26B)-C(27B)	1.463(8)
C(26B)-C(29B)	1.529(9)
C(27B)-C(28B)	1.534(10)
C(29B)-C(30B)	1.529(10)
C(30B)-C(31B)	1.521(10)
C(31B)-C(32B)	1.498(10)
N(1)-S(3)	1.613(4)
N(2)-S(3)	1.619(3)
Si-C(25B)#1	1.704(9)
Si-C(25A)#1	1.829(9)
Si-C(22)#1	1.867(5)
C(2)-C(1)-H(1A)	109.5
C(2)-C(1)-H(1B)	109.5
H(1A)-C(1)-H(1B)	109.5
C(2)-C(1)-H(1C)	109.5
H(1A)-C(1)-H(1C)	109.5
H(1B)-C(1)-H(1C)	109.5
C(1)-C(2)-C(3)	113.2(4)
C(1)-C(2)-H(2A)	108.9
C(3)-C(2)-H(2A)	108.9
C(1)-C(2)-H(2B)	108.9
C(3)-C(2)-H(2B)	108.9
H(2A)-C(2)-H(2B)	107.8
C(4)-C(3)-C(2)	113.0(3)
C(4)-C(3)-H(3A)	109.0
C(2)-C(3)-H(3A)	109.0
C(4)-C(3)-H(3B)	109.0
C(2)-C(3)-H(3B)	109.0
H(3A)-C(3)-H(3B)	107.8
C(3)-C(4)-C(5)	113.6(3)
C(3)-C(4)-H(4A)	108.8
C(5)-C(4)-H(4A)	108.8
C(3)-C(4)-H(4B)	108.8
C(5)-C(4)-H(4B)	108.8
H(4A)-C(4)-H(4B)	107.7
C(6)-C(5)-C(4)	110.9(4)
C(6)-C(5)-H(5A)	109.5
C(4)-C(5)-H(5A)	109.5
C(6)-C(5)-H(5B)	109.5
C(4)-C(5)-H(5B)	109.5
H(5A)-C(5)-H(5B)	108.0
C(7)-C(6)-C(5)	115.6(4)
C(7)-C(6)-H(6A)	108.4

C(5)-C(6)-H(6A)	108.4
C(7)-C(6)-H(6B)	108.4
C(5)-C(6)-H(6B)	108.4
H(6A)-C(6)-H(6B)	107.4
C(8)-C(7)-C(6)	130.4(4)
C(8)-C(7)-S(1)	110.4(3)
C(6)-C(7)-S(1)	119.1(3)
C(7)-C(8)-C(9)	113.1(5)
C(7)-C(8)-H(8)	123.4
C(9)-C(8)-H(8)	123.4
C(10)-C(9)-C(8)	113.8(4)
C(10)-C(9)-H(9)	123.1
C(8)-C(9)-H(9)	123.1
C(9)-C(10)-C(11)	131.7(4)
C(9)-C(10)-S(1)	109.8(3)
C(11)-C(10)-S(1)	118.5(3)
C(12)-C(11)-C(10)	128.4(3)
C(12)-C(11)-S(2)	110.4(3)
C(10)-C(11)-S(2)	121.2(3)
C(11)-C(12)-C(13)	114.6(4)
C(11)-C(12)-H(12)	122.7
C(13)-C(12)-H(12)	122.7
C(14)-C(13)-C(12)	112.3(4)
C(14)-C(13)-H(13)	123.8
C(12)-C(13)-H(13)	123.8
C(13)-C(14)-C(15)	128.1(4)
C(13)-C(14)-S(2)	110.6(3)
C(15)-C(14)-S(2)	121.3(3)
C(16)-C(15)-C(17)	114.7(3)
C(16)-C(15)-C(14)	122.2(4)
C(17)-C(15)-C(14)	123.1(4)
N(3)-C(16)-C(15)	126.3(4)
N(3)-C(16)-H(16)	116.9
C(15)-C(16)-H(16)	116.9
N(1)-C(17)-C(15)	127.6(4)
N(1)-C(17)-C(18)	112.3(4)
C(15)-C(17)-C(18)	120.1(4)
N(2)-C(18)-C(17)	114.0(3)
N(2)-C(18)-C(19)	127.0(4)
C(17)-C(18)-C(19)	119.0(4)
N(3)-C(19)-C(18)	119.7(3)
N(3)-C(19)-C(20)	117.6(4)
C(18)-C(19)-C(20)	122.8(4)
C(21)-C(20)-C(19)	130.7(4)
C(21)-C(20)-S(4)	111.5(3)
C(19)-C(20)-S(4)	117.8(3)
C(20)-C(21)-C(22)	114.2(4)
C(20)-C(21)-H(21)	122.9
C(22)-C(21)-H(21)	122.9
C(23)-C(22)-C(21)	110.4(4)
C(23)-C(22)-Si	108.3(3)
C(21)-C(22)-Si	141.3(4)
C(22)-C(23)-C(23)#1	116.1(2)
C(22)-C(23)-S(4)	113.4(3)
C(23)#1-C(23)-S(4)	130.53(14)
C(26A)-C(25A)-Si	131.8(9)

C(29A)-C(26A)-C(27A)	109.3(8)
C(29A)-C(26A)-C(25A)	109.5(8)
C(27A)-C(26A)-C(25A)	106.5(8)
C(26A)-C(27A)-C(28A)	109.3(9)
C(30A)-C(29A)-C(26A)	113.6(10)
C(29A)-C(30A)-C(31A)	112.5(10)
C(30A)-C(31A)-C(32A)	107.2(10)
C(26B)-C(25B)-C(25B)#1	154.6(12)
C(26B)-C(25B)-Si	100.0(7)
C(25B)#1-C(25B)-Si	60.1(4)
C(27B)-C(26B)-C(25B)	114.2(7)
C(27B)-C(26B)-C(29B)	111.6(8)
C(25B)-C(26B)-C(29B)	108.7(8)
C(26B)-C(27B)-C(28B)	112.2(8)
C(30B)-C(29B)-C(26B)	109.7(9)
C(31B)-C(30B)-C(29B)	108.1(10)
C(32B)-C(31B)-C(30B)	111.3(10)
C(17)-N(1)-S(3)	106.9(3)
C(18)-N(2)-S(3)	106.0(3)
C(19)-N(3)-C(16)	120.2(3)
C(7)-S(1)-C(10)	92.9(2)
C(11)-S(2)-C(14)	92.1(2)
N(1)-S(3)-N(2)	100.84(19)
C(23)-S(4)-C(20)	90.5(2)
C(25B)#1-Si-C(25B)	59.8(7)
C(25B)#1-Si-C(25A)	96.5(7)
C(25B)-Si-C(25A)	36.9(6)
C(25B)#1-Si-C(25A)#1	36.9(6)
C(25B)-Si-C(25A)#1	96.5(7)
C(25A)-Si-C(25A)#1	133.3(11)
C(25B)#1-Si-C(22)#1	126.6(5)
C(25B)-Si-C(22)#1	128.2(5)
C(25A)-Si-C(22)#1	104.3(5)
C(25A)#1-Si-C(22)#1	108.0(6)
C(25B)#1-Si-C(22)	128.2(5)
C(25B)-Si-C(22)	126.6(5)
C(25A)-Si-C(22)	108.0(6)
C(25A)#1-Si-C(22)	104.3(5)
C(22)#1-Si-C(22)	91.1(3)

Symmetry transformations used to generate equivalent atoms:

#1 -x,y,-z+1/2

Table S8. Anisotropic displacement parameters ($\text{\AA}^2 \times 10^3$) for DTS(PTTh₂)₂. The anisotropic displacement factor exponent takes the form: $-2\pi^2 [h^2 a^*{}^2 U^{11} + \dots + 2 h k a^* b^* U^{12}]$.

	U ¹¹	U ²²	U ³³	U ²³	U ¹³	U ¹²
C(1)	67(3)	59(3)	45(2)	4(2)	12(2)	-5(2)
C(2)	44(2)	53(3)	33(2)	-1(2)	7(2)	-5(2)
C(3)	39(2)	61(3)	32(2)	-3(2)	6(2)	-5(2)
C(4)	38(2)	60(3)	33(2)	-3(2)	5(2)	4(2)
C(5)	41(2)	64(3)	33(2)	0(2)	3(2)	7(2)
C(6)	46(2)	66(3)	36(2)	-1(2)	2(2)	9(2)
C(7)	42(2)	68(3)	36(2)	-2(2)	4(2)	10(2)
C(8)	49(2)	63(3)	48(3)	-3(2)	-2(2)	9(2)
C(9)	43(2)	76(3)	41(2)	-5(2)	-6(2)	7(2)
C(10)	30(2)	72(3)	31(2)	-2(2)	1(2)	9(2)
C(11)	27(2)	77(3)	24(2)	4(2)	1(1)	7(2)
C(12)	35(2)	74(3)	28(2)	1(2)	-3(2)	0(2)
C(13)	34(2)	75(3)	28(2)	3(2)	-1(2)	-1(2)
C(14)	28(2)	73(3)	24(2)	1(2)	3(1)	1(2)
C(15)	25(2)	68(3)	24(2)	0(2)	2(1)	2(2)
C(16)	30(2)	60(3)	32(2)	1(2)	2(2)	4(2)
C(17)	26(2)	69(3)	25(2)	-1(2)	4(1)	-4(2)
C(18)	28(2)	64(3)	26(2)	1(2)	5(1)	-4(2)
C(19)	24(2)	65(3)	26(2)	0(2)	3(1)	0(2)
C(20)	26(2)	69(3)	26(2)	-1(2)	-1(1)	-2(2)
C(21)	49(2)	60(3)	40(2)	-5(2)	-11(2)	-4(2)
C(22)	57(3)	59(3)	43(2)	-2(2)	-16(2)	1(2)
C(23)	30(2)	58(3)	30(2)	3(2)	-3(2)	3(2)
N(1)	36(2)	73(3)	29(2)	-4(2)	3(1)	-11(2)
N(2)	37(2)	72(3)	28(2)	0(2)	1(1)	-7(2)
N(3)	26(2)	70(3)	25(2)	-2(2)	-2(1)	2(2)
S(1)	44(1)	68(1)	29(1)	0(1)	-3(1)	13(1)
S(2)	33(1)	69(1)	27(1)	0(1)	-2(1)	5(1)
S(3)	49(1)	70(1)	32(1)	-5(1)	-2(1)	-11(1)
S(4)	24(1)	57(1)	24(1)	-1(1)	0(1)	2(1)
Si	182(3)	52(1)	82(2)	0	-83(2)	0

Table S9. Hydrogen coordinates ($\text{\AA} \times 10^4$) and isotropic displacement parameters ($\text{\AA}^2 \times 10^3$) for DTS(PTTh₂)₂.

	x	y	z	U(eq)
H(1A)	2843	-3252	17700	86
H(1B)	3242	-3144	18494	86
H(1C)	3146	-3202	16909	86
H(2A)	3262	-1738	17616	53
H(2B)	2955	-1789	18390	53
H(3A)	2840	-1919	15563	54
H(3B)	2536	-1946	16348	54
H(4A)	2969	-450	16255	53
H(4B)	2667	-476	17052	53
H(5A)	2542	-589	14213	56
H(5B)	2238	-630	15006	56
H(6A)	2384	814	15810	61
H(6B)	2684	854	15010	61
H(8)	1969	-11	12611	67
H(9)	1631	1043	11002	67
H(12)	1980	3858	12691	57
H(13)	1697	4986	11123	56
H(16)	1046	3422	7632	50
H(21)	568	6971	5446	63

Table S10. Torsion angles ($^{\circ}$) for DTS(PTTh₂)₂.

C(1)-C(2)-C(3)-C(4)	-178.6(4)
C(2)-C(3)-C(4)-C(5)	-179.5(3)
C(3)-C(4)-C(5)-C(6)	179.1(4)
C(4)-C(5)-C(6)-C(7)	-179.5(4)
C(5)-C(6)-C(7)-C(8)	-2.6(7)
C(5)-C(6)-C(7)-S(1)	-180.0(3)
C(6)-C(7)-C(8)-C(9)	-177.1(4)
S(1)-C(7)-C(8)-C(9)	0.4(5)
C(7)-C(8)-C(9)-C(10)	0.5(6)
C(8)-C(9)-C(10)-C(11)	176.3(4)
C(8)-C(9)-C(10)-S(1)	-1.2(5)
C(9)-C(10)-C(11)-C(12)	-174.9(5)
S(1)-C(10)-C(11)-C(12)	2.3(6)
C(9)-C(10)-C(11)-S(2)	3.7(6)
S(1)-C(10)-C(11)-S(2)	-179.1(2)
C(10)-C(11)-C(12)-C(13)	178.1(4)
S(2)-C(11)-C(12)-C(13)	-0.6(5)
C(11)-C(12)-C(13)-C(14)	-0.2(5)
C(12)-C(13)-C(14)-C(15)	-179.1(4)
C(12)-C(13)-C(14)-S(2)	1.0(4)
C(13)-C(14)-C(15)-C(16)	175.6(4)
S(2)-C(14)-C(15)-C(16)	-4.5(5)
C(13)-C(14)-C(15)-C(17)	-5.4(6)
S(2)-C(14)-C(15)-C(17)	174.5(3)
C(17)-C(15)-C(16)-N(3)	-1.9(6)
C(14)-C(15)-C(16)-N(3)	177.2(4)
C(16)-C(15)-C(17)-N(1)	-178.4(4)
C(14)-C(15)-C(17)-N(1)	2.5(6)
C(16)-C(15)-C(17)-C(18)	2.1(5)
C(14)-C(15)-C(17)-C(18)	-177.0(3)
N(1)-C(17)-C(18)-N(2)	-1.3(5)
C(15)-C(17)-C(18)-N(2)	178.3(3)
N(1)-C(17)-C(18)-C(19)	179.6(3)
C(15)-C(17)-C(18)-C(19)	-0.8(5)
N(2)-C(18)-C(19)-N(3)	-179.8(4)
C(17)-C(18)-C(19)-N(3)	-0.9(5)
N(2)-C(18)-C(19)-C(20)	0.4(6)
C(17)-C(18)-C(19)-C(20)	179.3(3)
N(3)-C(19)-C(20)-C(21)	-179.0(4)
C(18)-C(19)-C(20)-C(21)	0.8(7)
N(3)-C(19)-C(20)-S(4)	1.3(5)
C(18)-C(19)-C(20)-S(4)	-178.9(3)
C(19)-C(20)-C(21)-C(22)	-179.7(4)
S(4)-C(20)-C(21)-C(22)	0.0(5)
C(20)-C(21)-C(22)-C(23)	0.0(6)
C(20)-C(21)-C(22)-Si	-176.7(5)
C(21)-C(22)-C(23)-C(23) ^{#1}	179.9(5)
Si-C(22)-C(23)-C(23) ^{#1}	-2.2(6)
C(21)-C(22)-C(23)-S(4)	-0.1(5)
Si-C(22)-C(23)-S(4)	177.7(2)
Si-C(25A)-C(26A)-C(29A)	-169.4(14)
Si-C(25A)-C(26A)-C(27A)	-51.4(18)

C(29A)-C(26A)-C(27A)-C(28A)	40(2)
C(25A)-C(26A)-C(27A)-C(28A)	-78.6(19)
C(27A)-C(26A)-C(29A)-C(30A)	116(2)
C(25A)-C(26A)-C(29A)-C(30A)	-128(2)
C(26A)-C(29A)-C(30A)-C(31A)	47(4)
C(29A)-C(30A)-C(31A)-C(32A)	-145(3)
C(25B)#1-C(25B)-C(26B)-C(27B)	101(3)
Si-C(25B)-C(26B)-C(27B)	64.7(11)
C(25B)#1-C(25B)-C(26B)-C(29B)	-134(3)
Si-C(25B)-C(26B)-C(29B)	-169.9(10)
C(25B)-C(26B)-C(27B)-C(28B)	58.7(18)
C(29B)-C(26B)-C(27B)-C(28B)	-65(2)
C(27B)-C(26B)-C(29B)-C(30B)	-156(3)
C(25B)-C(26B)-C(29B)-C(30B)	78(3)
C(26B)-C(29B)-C(30B)-C(31B)	-168(3)
C(29B)-C(30B)-C(31B)-C(32B)	-177(3)
C(15)-C(17)-N(1)-S(3)	-178.5(3)
C(18)-C(17)-N(1)-S(3)	1.1(4)
C(17)-C(18)-N(2)-S(3)	0.9(4)
C(19)-C(18)-N(2)-S(3)	179.9(3)
C(18)-C(19)-N(3)-C(16)	1.1(5)
C(20)-C(19)-N(3)-C(16)	-179.1(3)
C(15)-C(16)-N(3)-C(19)	0.3(6)
C(8)-C(7)-S(1)-C(10)	-0.9(4)
C(6)-C(7)-S(1)-C(10)	177.0(4)
C(9)-C(10)-S(1)-C(7)	1.2(4)
C(11)-C(10)-S(1)-C(7)	-176.6(3)
C(12)-C(11)-S(2)-C(14)	1.0(3)
C(10)-C(11)-S(2)-C(14)	-177.8(3)
C(13)-C(14)-S(2)-C(11)	-1.1(3)
C(15)-C(14)-S(2)-C(11)	179.0(3)
C(17)-N(1)-S(3)-N(2)	-0.5(3)
C(18)-N(2)-S(3)-N(1)	-0.2(3)
C(22)-C(23)-S(4)-C(20)	0.1(4)
C(23)#1-C(23)-S(4)-C(20)	-180.0(5)
C(21)-C(20)-S(4)-C(23)	-0.1(3)
C(19)-C(20)-S(4)-C(23)	179.7(3)
C(26B)-C(25B)-Si-C(25B)#1	163.1(16)
C(26B)-C(25B)-Si-C(25A)	-10.1(9)
C(25B)#1-C(25B)-Si-C(25A)	-173.1(18)
C(26B)-C(25B)-Si-C(25A)#1	167.2(8)
C(25B)#1-C(25B)-Si-C(25A)#1	4.1(11)
C(26B)-C(25B)-Si-C(22)#1	48.3(10)
C(25B)#1-C(25B)-Si-C(22)#1	-114.8(8)
C(26B)-C(25B)-Si-C(22)	-79.7(9)
C(25B)#1-C(25B)-Si-C(22)	117.3(8)
C(26A)-C(25A)-Si-C(25B)#1	-48.7(16)
C(26A)-C(25A)-Si-C(25B)	-42.8(14)
C(26A)-C(25A)-Si-C(25A)#1	-46.5(14)
C(26A)-C(25A)-Si-C(22)#1	-179.1(14)
C(26A)-C(25A)-Si-C(22)	84.9(16)
C(23)-C(22)-Si-C(25B)#1	-139.9(6)
C(21)-C(22)-Si-C(25B)#1	36.9(9)
C(23)-C(22)-Si-C(25B)	142.4(6)
C(21)-C(22)-Si-C(25B)	-40.8(9)
C(23)-C(22)-Si-C(25A)	106.2(6)

C(21)-C(22)-Si-C(25A)	-77.1(8)
C(23)-C(22)-Si-C(25A)#1	-108.1(7)
C(21)-C(22)-Si-C(25A)#1	68.7(9)
C(23)-C(22)-Si-C(22)#1	0.8(2)
C(21)-C(22)-Si-C(22)#1	177.5(8)

Symmetry transformations used to generate equivalent atoms:

#1 -x,y,-z+1/2